

FINAL YEAR PROJECT REPORT

NAME:	James Paget
DEGREE COURSE:	Mathematics and Physics MSci
PROJECT TITLE:	Applying a bead and spring framework to light-driven deformation
YEAR OF SUBMISSION:	2025
SUPERVISOR:	Dr. Simon Hanna
NUMBER OF WORDS:	6569



Declaration

All data given was collected by my partner and I unless otherwise stated. The DDA simulation run to collect our results was provided to us by our supervisor Dr. Simon Hanna, but had to be modified to acquire the results found during the project, mainly in the calculation of forces (spring and bending) between a set of particles, which we generalised to consider a set of particles without having assumed 1D connections. We also generalised the consideration of particles of different sizes and dipole generation configurations (referred to as primitives), as well as some additions to the hydrodynamics, most of which was already implemented. The additional files *SimulationVary.py* and *Generate_yaml.py* were also created specifically for this project. The core DDA calculation for the optical forces and fields for each particle was not changed significantly. Several ideas for experimentation were suggested by our supervisor in our weekly meetings. Myself and my partner, David Tudor, equally shared work in terms of the programming as well as analysis of data, working closely together to assist each other in the writing of code and interpretation of results, however our final analysis of the data was performed separately and may differ. All graphs, unless otherwise stated, were generated using code written together.

Acknowledgements

I would like to thank my project partner David Tudor for all his contributions to the program we worked on and the countless discussions we have had to enhance my understanding of the project. I also would like to thank Dr. Simon Hanna for his guidance and support during our weekly meetings and the numerous insights he provided about the field and how to approach research as a whole.

Abstract

The validity of the bead and spring model has been assessed for DDA optical scattering simulations and shown to be in good agreement with experimental observations. Modelling a simple red blood cell with a bead and spring membrane framework inside an optical stretcher setup has demonstrated valid deformation with minimal volume loss after reaching a stable deformed equilibrium. Several connection regimes have also been considered for modelling micro-rods, which generated a range of deflections by varying structural parameters, allowing tunable flexibility.

Contents

1	Introduction	4
2	Theory	4
2.1	DDA Simulation	4
2.2	Bead-and-Spring Models	6
2.3	Dynamics	7
2.4	Shaped Beams & Manipulation Techniques	8
2.5	Abraham-Minkowski Controversy	10
3	Experimental Validation	11
3.1	Single dipoles	11
3.2	Sphere-Cube Convergence	13
3.3	Sphere and Torus Models	15
4	Experimental Application	18
4.1	Rod Deformation Models	18
4.2	Optical Stretchers	20
5	Conclusions	28
6	Appendices	28

1 Introduction

Simulating the electromagnetic fields generated from light scattering interactions within a material can be found through one of several techniques such as the discrete dipole approximation (DDA), T-Matrix method and finite-difference time-domain method (FDTD), however each of these are only valid when the relevant optical objects are rigid (their geometry cannot be deformed). Interest in the effects of light scattering for deformable objects peaked after Arthur Ashkin published his Nobel prize winning paper on the optical manipulation of micro-particles[1], which prompted a field of medical research making use of these so called optical tweezers to probe characteristics of biological materials through imposed optical forces.

Red blood cells (RBC) have been experimentally stretched through optical means to determine their elasticity, in turn characterising whether the cell is healthy or afflicted by some condition, such as sickle cell disease[2], which requires the precision of an optical measurement to accurately resolve the forces involved. Similarly, DNA stretching has also lead to discoveries about its properties, wherein its flexibility played a critical role in this behaviour[3].

More efficient and accessible medical research could be performed if a simulation were able to correctly model these essential flexible characteristics in the presence of optical interactions, as opposed to requiring the complex setup and tuning of physical optical tweezers apparatus. Such a simulation would allow ordinarily difficult measurements to be performed, such as for molecules which are delicate or hard to acquire in abundance.

Currently DDA has been applied to study cases

such as the interaction of dust particulates[4] and human blood neutrophil characteristics[5], with some efforts to generalise its methodology for flexible scenarios, such as using granular[6] dipoles rather than lattice based objects to allow a wider range of dipole positioning with less geometry dependence, or in the consideration of particles in an electrorheological fluid as point dipoles which give rise to aggregation in light scattering simulations[7]. Both cases do not consider single, deformable bodies but do explore systems of dipoles that are less constrained to some fixed, rigid space. However, bead and spring models have been extensively used in biological polymer applications[8] for optically opaque particles, and so the aims of this project are to validate whether such a model could be applied in optically dense scenarios when using the DDA method of light scattering calculation, as well as to experimentally assess the accuracy of the combination of these techniques for known systems.

2 Theory

2.1 DDA Simulation

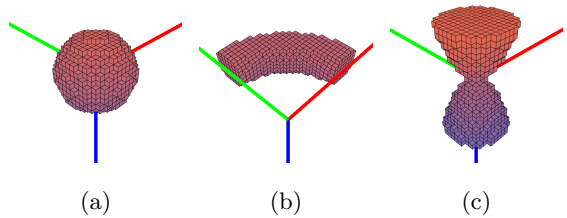


Figure 1: Examples of discrete voxelisation of shapes for usage in a DDA scattering simulation. **(a)** – **(c)** represent a modelled sphere, torus sector and an arbitrary shape. The XYZ axes are shown to help visualise the 3D shape, as well as a colour gradient displaying the negative Z height of each dipole relative to the origin.

Light acting from an external beam can be have its scattered field simulated through usage of the Discrete Dipole Approximation (DDA), which is also known as the Coupled Dipole Method in other literature[9]. Fundamentally this method treats the atoms present within a material as dipolar voxels (cubic volume elements) which do not intersect, as depicted in figure 1, wherein each dipole scatters the field incident on it producing additional electric field contributions over every other dipole, causing further scattering. For consistency, the term 'particle' will refer to the primitive shapes (such as spheres and cubes) modelled through these dipoles, and 'mesh' will refer to a collection of particles within a given system. For simplicity, the DDA formulation used treats the material as non-magnetic (assuming a stronger electric interaction), and assumes a linear response to incident electric fields, $\mathbf{E}_i(\mathbf{r}_i) = \mathbf{P}_i/\alpha$, for an electric field \mathbf{E} , dipole polarisation \mathbf{P} and polarisability α for the i^{th} dipole, where the polarisability has been taken to be a constant for an assumed homogenous material (however, generalisation of this concept to a tensor can also be considered[9]). Calculating the electric field incident on each dipole is the contribution from both the external beam as well as interacting components from every other dipole's scattered light, resulting in the formulation[10][11];

$$\mathbf{E}_{int} = \mathbf{E}_{inc} + \sum_i \bar{\mathbf{G}} \cdot \mathbf{P}_i, \quad (1)$$

$$\begin{aligned} \bar{\mathbf{G}} = \frac{\exp(ikR)}{R} & [k^2(\bar{\mathbf{I}} - \frac{\bar{\mathbf{R}} \otimes \bar{\mathbf{R}}}{R^2}) - \\ & \frac{1 - ikR}{R^2}(\bar{\mathbf{I}} - 3\frac{\bar{\mathbf{R}} \otimes \bar{\mathbf{R}}}{R^2})], \end{aligned} \quad (2)$$

for a wave-number k , relative displacement \mathbf{R} (be-

tween the target and iterated dipoles) and where \otimes represents the dyadic product between two vectors (which combines the two vectors into a matrix). $\bar{\mathbf{G}}$ refers to the Green's interaction tensor which describes the scattering contribution experienced from the i^{th} dipole at a separate dipole, which decays to zero influence when dipoles are separated, as expected. Solving this series of equations simultaneously for the polarisations then allows the electric field to be found at each dipole. For a simple polarisability prescription, one can use the Clausius-Mossotti (CM) relation[9];

$$\alpha_{cm} = \frac{3d^3}{4\pi} \frac{\epsilon_n - \epsilon_m}{\epsilon_n + 2\epsilon_m}, \quad (3)$$

given that d is the diameter of the dipole, and ϵ_n and ϵ_m are the dielectric constants (given by $\epsilon_n = n^2$) for the particle and surrounding medium respectively, describing how refractive media are polarised in response to an electric field. However, improved models exist which include the recursive, self-interacting addition from the re-scattered fields (between dipoles) observed once again at an initially chosen dipole, leading to an additional imaginary polarisability term which will perform a critical role in sections 3.1 and 4 when forces are being calculated [12]. Usage of the radiative reaction (RR) polarisability

$$\alpha_{RR} = \frac{\alpha_{cm}}{1 - \frac{2}{3}ik^3\alpha_{cm}}, \quad (4)$$

applies this correction which works particularly well for smaller magnitudes of refractive indices considered. Dealing with more refractive material requires use of the lattice dispersion relation (LDR), which conceptually works like RR (equation given in appendices A), however many other forms have

also had their effectiveness evaluated[9].

Once all electric fields are known at each dipole, the time averaged force, $\langle \mathbf{F} \rangle$, exerted on each dipole can be found through the application of[13]

$$\begin{aligned} \mathbf{F} = & \sum_i^N \frac{1}{4} \alpha_1 \nabla |E|^2 - \alpha_2 \left(\frac{1}{2} \text{Im}(\mathbf{E}_i \times (\nabla \times \mathbf{E}^*)) \right. \\ & \left. - \frac{i}{4} \nabla \times (\mathbf{E}_i \times \mathbf{E}_i^*) \right), \\ \alpha = & \alpha_1 + i\alpha_2 | \alpha_1, \alpha_2 \in \mathbb{R}, \end{aligned} \quad (5)$$

which reduces to a more compact result in the non-absorbing case[12]

$$\langle \mathbf{F}_i \rangle = \frac{1}{2} \text{Re} \left(\sum_j \mathbf{P}_j \partial_i \mathbf{E}_j^* \right), \quad (6)$$

where N is the number of dipoles and α_1, α_2 give the real and imaginary parts of the polarisability of the dipole. Hence by summing the forces over all dipoles composing a particle the total optical force exerted can be found. When the number of dipoles considered is taken to be infinitely large, DDA has been proven to give numerically exact calculations[14], meaning the results found through DDA for large dipole numbers becomes increasingly accurate given the underlying assumptions such as $d < \lambda/(10|n|)$ [9], where d is the diameter of each dipolar voxel, n is the refractive index and λ is the wavelength of the acting light beam, so dipoles are substantially small relative to the incident light's wavelength such that the electric field within a dipole is approximately constant.

2.2 Bead-and-Spring Models

Modelling an object with beads and springs requires the discretisation of the object into simplified par-

ticles which can then be bound together through a set of forces transferred through connections between these particles. Since the optical forces can be found using DDA, the complete simulation must apply additional forces by considering the connections in our model. When given a set of connections between particles, the spring forces can simply be found through the application of Hooke's law

$$\mathbf{F}_{\text{elastic}} = k_{\text{spring}}(r - l)\hat{\mathbf{r}}, \quad (7)$$

where k_{spring} is the spring constant, l is the natural length of the spring and $r, \hat{\mathbf{r}}$ give the magnitude and direction of the displacement between two connected particles, where these parameters may be unique for each connection. As well as this, each combination of 3 adjacent connections can have a unique equilibrium angle, θ_{eqm} , assigned to it, wherein a normal restoring force (derived from a restoring potential[15]) will be applied to each connected particle if this angle is offset, in accordance with the formula:

$$\begin{aligned} \mathbf{F}_{i, \text{bending}} &= k_{\text{bending}} \left(\frac{\cos(\theta_{ijk}) \mathbf{r}_{ji}}{r_{ji}^2} - \frac{\mathbf{r}_{jk}}{r_{ji} r_{jk}} \right), \\ \mathbf{F}_{k, \text{bending}} &= k_{\text{bending}} \left(\frac{\cos(\theta_{ijk}) \mathbf{r}_{jk}}{r_{jk}^2} - \frac{\mathbf{r}_{ji}}{r_{ji} r_{jk}} \right), \end{aligned} \quad (8)$$

$$\mathbf{F}_{j, \text{bending}} = -(\mathbf{F}_{i, \text{bending}} + \mathbf{F}_{k, \text{bending}}),$$

where θ_{ijk} is the angle between the 3 particles (j always central), k_{bending} is a constant expressing the influence of the bending force and \mathbf{r}_{pq} are the displacements between the p^{th} and q^{th} particles in this set, where the i^{th}, j^{th} and k^{th} particles are located as depicted in figure 2, except the vector \mathbf{r}_{ij} is rotated by θ_{eqm} immediately first to convert the angular equilibrium back to a flat line equilibrium, which is where the equation above is valid.

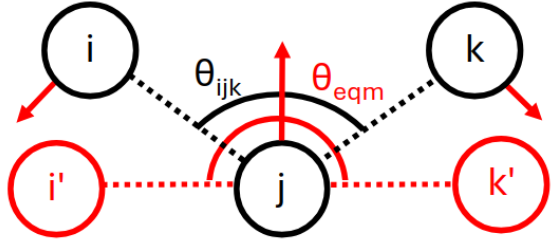


Figure 2: Diagrammatic example of how calculated bending forces move particles towards an assigned equilibrium angle for every set of 3 adjacent connected particles. The equilibrium angle, $\theta_{eqm} = \pi$ here, but in general is arbitrary. θ_{ijk} represents the angle between the particles in the system currently. The red arrows represent the bending force applied to particles, and the dotted lines represent the connections between particles.

Additional forces may also be considered[15], such as torque terms, however for the experimental procedures covered within this project just the spring and bending forces were deemed to dominate.

Simulation work in section 3 onwards will utilise a modified implementation of DDA software to include particle dynamics as well, provided by Dr. Simon Hanna which was then extended. Open source software ADDA[9][16] was also trialled for usage here, however lacked the appropriate framework to work with multiple particles and calculate forces for beam profiles required (more information on this in appendix B).

2.3 Dynamics

Numerically the dynamics for a system can be found if all the acting forces are known and a differential equation can be constructed. Within the following DDA simulations particles can have arbitrary material properties but the surrounding medium will always be taken to have a refractive index $n = 1.33$

to simulate water, and so will include drag forces. By considering the particles to be in a low Reynolds number regime, $Re = \frac{UL}{\nu} \ll 1$, which is reasonable since the particles considered have small width and velocity (order $10^{-6}m$ diameter and particles often travel approximately $10^{-7}m$ for $dt = 10^{-4}s$, hence their velocity is also of the small order $10^{-3}ms^{-1}$), therefore inertial terms involved in our equation of motion can be ignored. Using Newton's 2nd law and equating the remaining forces here to the drag force, in order to form a differential equation as this force is velocity dependent, then requires the particle always be in equilibrium requiring it to be at terminal velocity every time-step. Sufficient time must be allowed for the particle's motion to experience a damping force (so acceleration is $0ms^{-2}$), but not so large that unphysical gradient jumps are incurred each step. Equally, for very small time-steps ($dt \approx 10^{-7}s$) Brownian motion has been observed to have a ballistic trajectory[17], which would contradict our statistical calculations used. Applying these ideas we acquire an approximate bound for the time-step $dt \in (10^{-7}, 10^{-4})s$ and an equation of motion[18];

$$\begin{aligned} \mathbf{r}_i &= \mathbf{r}_i^0 + \sum_j \frac{\partial \bar{D}_{ij}^0 \mathbf{F}_j^0}{\partial \mathbf{r}_j} \Delta t + \mathbf{R}_i(\Delta t), \\ \bar{D}_{ij}^0 &= \frac{k_b T}{6\pi\eta a} \delta_{ij} |i = j, \\ &= \frac{k_b T}{8\pi\eta a} \left(\bar{\mathbf{I}} + \frac{\mathbf{r}_{ij} \otimes \mathbf{r}_{ij}}{\mathbf{r}_{ij}^2} \right) |i \neq j, \end{aligned} \quad (9)$$

along with

$$\mathbf{R}(\Delta t) = \left(\frac{k_b T}{3\pi\eta a} \Delta t \right)^{\frac{1}{2}} \mathbf{R}, \quad (10)$$

where k_b , T , η and a are the Boltzmann con-

stant, fluid temperature, dynamical viscosity and the spherical particle's radius, respectively, and δ_{ij} , \bar{I} , \mathbf{r}_{ij} and \mathbf{R} are the Kronecker delta function for the i^{th} and j^{th} particle coordinates, the identity matrix, the displacement between two particle positions and a normally distributed random variable, respectively. This is the critical equation governing the motion of particles in the dynamics simulation which accounts for drag, Brownian motion and the totalled forces $\mathbf{F}^0 = \mathbf{F}_{optical} + \mathbf{F}_{Spring} + \mathbf{F}_{Bending}$ experienced by particles within the system. As well as this, a Buckingham force may also be included which accounts for inter-molecular attraction and repulsion, however due to the close proximities considered in section 3 this term can often result in unstable behaviour (this would be more relevant if multiple meshes were being considered at once, however this will not be considered here), and so will only be included in the appendices C.

2.4 Shaped Beams & Manipulation Techniques

Experimental work in sections 3 onwards will require the use of several beam types in order to manipulate particles with various optical tools. Therefore these ideas will be briefly introduced here to facilitate investigation later.

Gaussian beams are often used for experiments due to the simplicity of their beam shape and field gradients, as observed in the intensity plot 3a, which can be tuned by varying the wavelength, λ , and beam strength, E_0 , to optically trap particles at their focus. Optical trapping refers to the constraint of an object's position through the balance of gradient and scattering forces, as described in equation 5. This results in a minimised potential

by moving the particle into the high intensity section of a beam (to cancel the gradient force across its surface with the overall scattering force experienced).

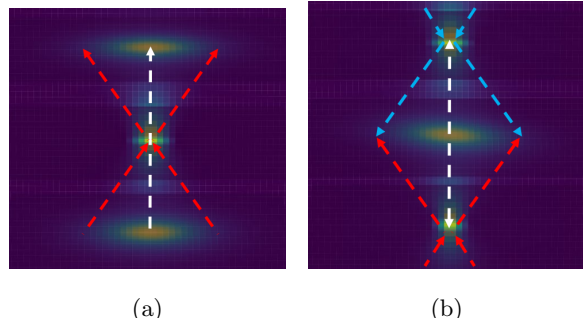


Figure 3: Depicts the intensity field of two setups using Gaussian beams (1 beam for (a) and 2 counter propagating beams for (b)). The viewing axis is sampled at 3 points along the Z axis (propagation axis) and once in the X-Z plane, which are then layered and tilted to allow the entire 3D structure of the beam to be visualised at once. White arrows show the beam propagation directions, and the coloured arrows represent where the light from each beam travels. (a) plots the Gaussian beam intensity with the focus at the origin, where a high intensity convergence is seen at the origin, and diverging behaviour either side. (b) shows 2 counter-propagating Gaussian beams with foci offset either side of the Z-axis, similarly showing convergence at the foci and divergence otherwise. Wavelength $\lambda = 1 \times 10^{-6}m$ is used.

Combinations of these beams can be considered, such as with two counter-propagating Gaussian beams 3b with X and Y polarisations to prevent fringe interference behaviour occurring. The radiation pressure from the beams cancel and field gradients pull particles towards the central focus, or by separating the foci can create an optical stretcher. Optical stretchers follow the same principles of the

optical trapper, however trapping now competes between two separate Gaussian foci, leaving an imbalance in gradient forces on either side of a particle's surface. For a rigid particle, this will continue to trap at the origin, but for deformable particles this generates a tensile force (core principle behind section 4.2).

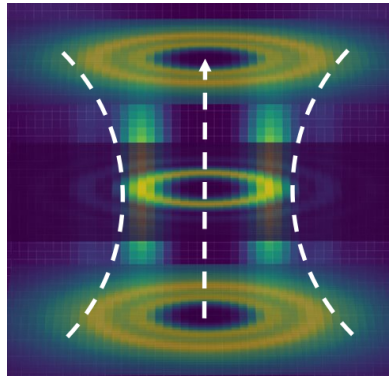


Figure 4: Setup as described in figure 3. A Laguerre-Gaussian beam is depicted with radial and azimuthal orders $p = 0, l = 3$. Fringes can be observed, as well as slight decay in the annulus radius as $Z = 0$ is approached from either side. Wavelength $\lambda = 1 \times 10^{-6}m$ is used.

Laguerre-Gaussian (LG) beams, also referred to as doughnut beams, have an intensity pattern as seen in figure 4. They can be described with a radial and azimuthal order p and l denoting the spin and orbital angular momentum[19] possessed by the beam, respectively, resulting in helical wavefronts[20] which evolve over time and impart spin or orbital angular momentum to optically trapped particles depending on their size relative to the beam width. Orbital motion that is confined to the high intensity annulus can then occur, which is used in optical pump setups, which direct fluid using the shear forces of orbiting beads (figure 5, which makes use of the large limit of particles in a beam which

will be explored in section 3.3).

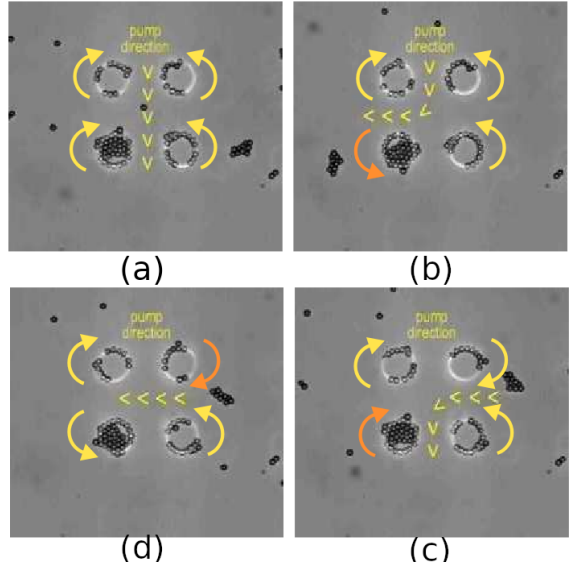


Figure 5: Figure reproduced from[21]: Jesacher, Alexander, et al. "Holographic optical tweezers for object manipulations at an air-liquid surface." Optics express 14.13 (2006): 6342-6352. Depicts the direction of fluid flow due to shear forces from orbiting particles in Laguerre-Gaussian beams creating an 'optical pump' setup to direct fluid flow. Each panel shows how varying flows can be generated.

Bessel beams will only briefly be considered but offer the advantages of the LG beam without having a Z field gradient (non-diffracting), making them ideal for special cases where the radiation pressure (acting along the Z axis in this case, but perpendicular to the intensity rings in general) needs to act in a direction independent of the field gradient, as can be seen in figure 6. For this reason they will play an important role in section 3.1 that neither a Gaussian or LG beam offer.

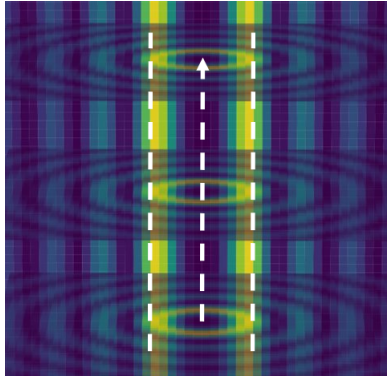


Figure 6: Setup as described in figure 3. An order 3 Bessel beam is depicted. Fringes can be observed with a consistent intensity across the Z-axis. White arrows show the propagation direction and gradient of the high intensity rings observed. Wavelength $\lambda = 0.4 \times 10^{-6} m$ is used.

The power for a Gaussian beam can also be found using[22][23]

$$P = \frac{1}{4}c\epsilon_0\pi w_0^2 E_0^2, \quad (11)$$

where c is the speed of light in a vacuum, ϵ_0 is the permittivity of free space, w_0 is the beam width and E_0 is the field strength at the beam's peak value. This will be used in section 4.2 to match simulated beam powers to experimental values.

2.5 Abraham-Minkowski Controversy

Max Abraham and Hermann Minkowski independently developed two separate formulations for the momentum density of light in refractive media[24] which supported opposing proportionalities to the refractive index, n . Both the Abraham and Minkowski forms are given by

$$\mathbf{P}_A = \int dV \frac{\mathbf{E} \times \mathbf{H}}{c^2}, \quad (12)$$

and

$$\mathbf{P}_M = \int dV \mathbf{D} \times \mathbf{B} = \int dV \frac{\mathbf{E} \times \mathbf{H}}{c^2} n^2 = n^2 \mathbf{P}_A, \quad (13)$$

which clearly differ by a factor of n^2 and both have supporting experimental evidence [25][26], hence leading to confusion as to which is valid, where for the equations above the \mathbf{E} and \mathbf{D} are the electric and displacement fields, \mathbf{B} and \mathbf{H} are the magnetic and magnetising fields, \mathbf{P} is either the Abraham or Minkowski form of the total momentum of a material being integrated over and c refers to the speed of light in a vacuum. In 2010 Stephen Barnett proposed a solution[20], stating that both formulas are correct, corresponding to a kinetic and canonical component of the total momentum. The total conserved momentum will always be experimentally measured, however the specific procedure of the experiment will affect the magnitude of each of these components, resulting in what appears to be contradictory regimes if one component is small relative to the other[27]. Others such as Masud Mansuripur have also argued[28] that simply applying Maxwell's equations with consideration to keep track of all momenta in the system (such as transferred components to a fluid an object is immersed within, or distributed throughout a glass block of varying transparency) then no additional considerations need to be made.

These perspectives suggest that both formulations of momentum density are required for the total momentum conservation to be valid. Optical force calculations within the simulation used in this project are derived from Maxwell's stress tensor (MST)[12] and so, as suggested, should have both the Abraham and Minkowski contributions included, and

so should have the correct total momentum density. Therefore given that neither momentum components are considered separately, as has historically been of significant concern and the primary issue with this controversy, the forces found for each dipole should not be conflicting and equally the volume integral for the particle's total force should have no issue.

3 Experimental Validation

It is non-trivial to assess whether a bead and spring model is applicable to light scattering simulations as, unlike a tradition bead and spring model, the dynamics of each particle is dependent on the entire system not just nearest neighbour connections. Therefore before simulations using an optical bead and spring model can be conducted the validity of this approach must be determined for limiting cases of significantly small and close particles, as is one of the core aims of the project, and so each of these experiments will be explained, experimented and analysed in turn, as successive experiments here require the prior to hold.

3.1 Single dipoles

One such example of this limiting case is where the refinement of the system, that is the number of dipoles approximating each particle and number of particles approximating the total mesh, is reduced to have just a single dipole per particle resulting in no radiation forces here (for a non-self interacting polarisability) due to the existence of this force within a DDA framework stemming from scattering interactions between other dipoles (summing over dipoles during calculation 5) and there

being no requisite imaginary polarisability component in, for example, a standard Clausius-Mossotti polarisability. Without an imaginary polarisability, each dipole will simply experience a gradient force from the total field. Therefore it must be validated that this effect is removed when considering appropriate polarisabilities such that a single dipole exhibits the same overarching behaviour of dipole clusters, so the radiation pressure is not entirely ignored, but notably with less field strength than may be expected due to the losses from a lower accuracy DDA model.

Investigating this effect, figure 7 shows how the force acting on a dipole varies as it is placed at different points across the beam, clearly showing that without this self-interacting polarisability an unphysical zero radiation pressure can be observed for single dipoles (7c), which is resolved after reintroducing even a small sample of nearby dipoles (a single dipole surrounded by 6 adjacent was considered in this case). Considering the RR and LDR cases, a Z force was experienced by both the single and grouped dipoles, demonstrating the expected collective behaviour within just a single dipole, as would be hoped. In addition, the RR has larger magnitudes for the Z forces observed, but very similar X and Y forces to the CM version since the X and Y forces are dominated by the electric field gradient, however the Z force is not, meaning the additional scattering introduced within this term gives the most significant change to this Z component. Note that the experimental procedure of moving the particle through the beam itself was not of importance, but rather just the observation that, when immersed in the beam, a large radiation pressure is generated due to this self-scattering.

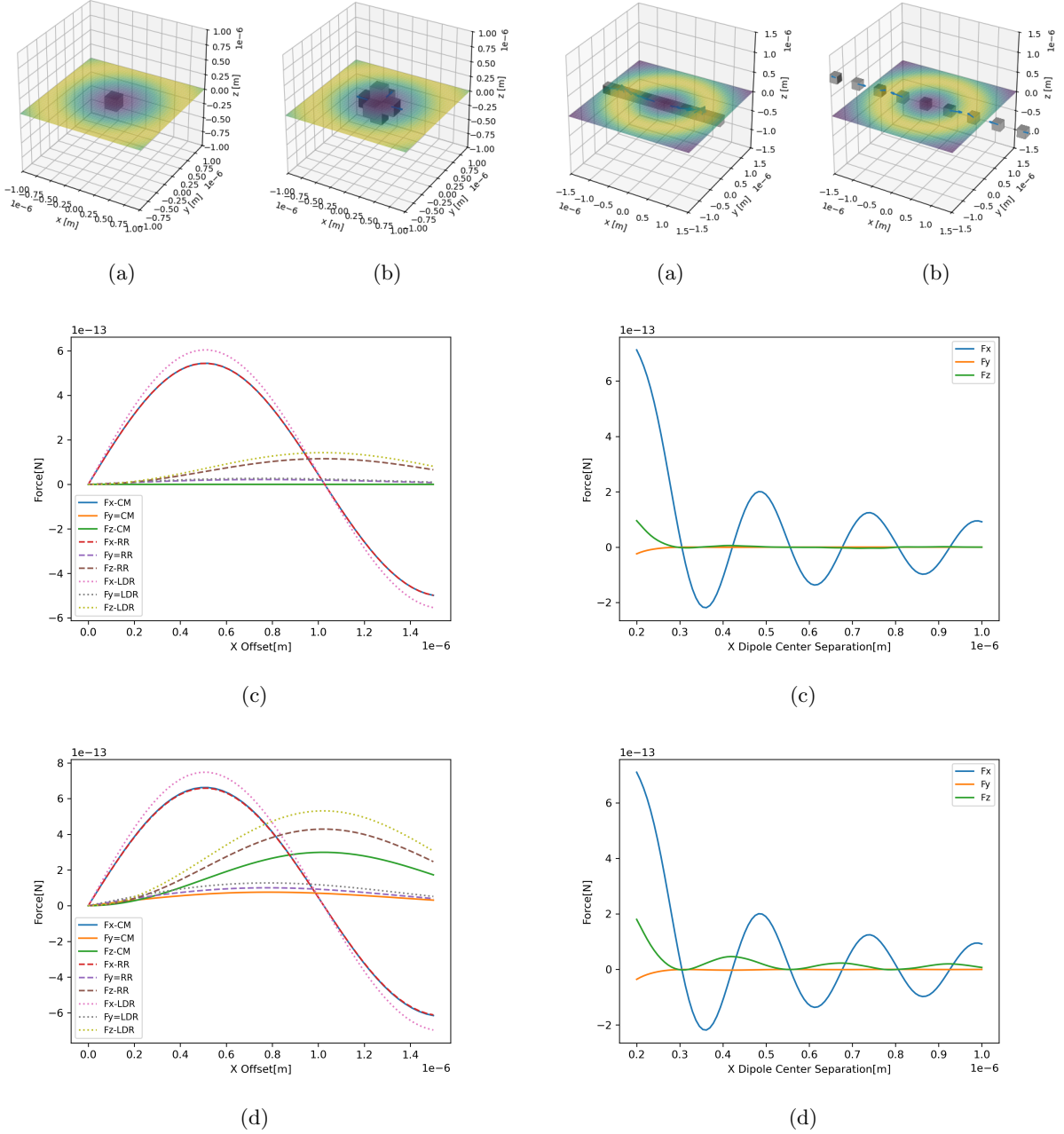


Figure 7: (a) and (b) show the initial position of a single dipole and 7 dipole mesh, respectively, within a Bessel beam. (c) and (d) show the XYZ components of the total optical force experienced by the mesh in the single and 7 dipole cases respectively as each mesh is translated through the space along the X axis, where each particle uses either the Clausius-Mossotti (CM), radiative reaction (RR) or lattice dispersion relation (LDR) as its polarisability prescription. Particles used have a particle and dipole radius of $R_p = R_d = 100\text{nm}$.

Figure 8: (a)-(b) depicts the setup of single dipole particles spread along the X axis with some varying separation inside a Bessel beam. (c) and (d) show the total optical force experienced by the left-most particle (0^{th} index) as the separation between each particle is changed, performed for the Clausius-Mossotti (CM) and radiative reaction (RR) polarisabilities respectively. Particles used have particle and dipole radii $R_p = R_d = 100\text{nm}$.

Similarly, by considering the force on a single dipolar particle as a group is separated we consider at

which length scales the correcting polarisability's influence changes, hence by comparison of 8c and 8d for separations less than $0.3\mu m$ the two formulations have significant agreement in behaviour, with the Clausius-Mossotti form having a reduced (approximately half the Z component) magnitude seen for the RR form, and for larger separations the systems clearly diverge from each other. Therefore these results imply the bead and spring model should show the correct behaviour even in the limiting case of a mesh being split into single dipole particles given that either the RR prescription is used or particles are sufficiently close. Similarly, the LDR prescription also accounts for this self-interaction and so gives the same results (as seen in figure 7). Interestingly, if particles are close enough (within the $0.3\mu m$ limit) then the use of either the CM or RR formulations should show the correct behaviour, hence for tight enough binding of particles problems would not be expected for single dipole particles using either polarisability, however the magnitude difference from the correcting factor would result in a noticeable change in force, and so RR will always be applied over the CM form.

3.2 Sphere-Cube Convergence

A crucial assumption in our dynamics calculation is that particles used are spherical (otherwise their drag force would require a different diffusion constant, as well as rotational considerations), hence particles forming any given mesh must be spherical if time-stepping dynamics are to be used. Therefore the optical properties of spherical beads must correspond to the properties of the object being modelled (the forces arising from spring connections will be verified in sections 4.1-4.2). Whilst DDA is nu-

merically exact when refining the dipoles per particle, this does not guarantee exact convergence for a refined space of particles (particles per mesh increased), and so must be confirmed as well.

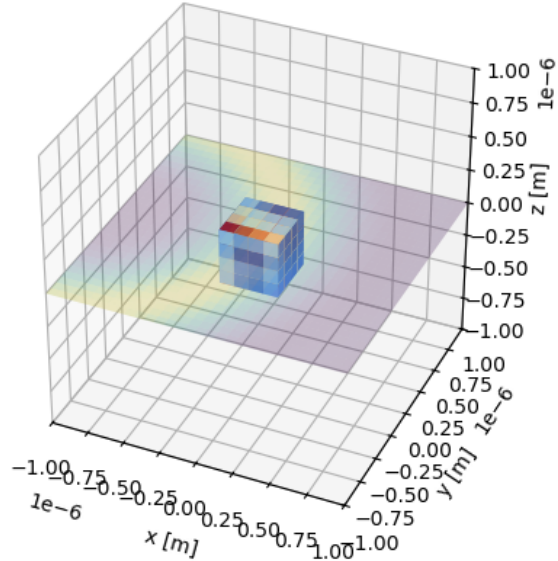


Figure 9: A cubic mesh of total half-width $R_m = 200nm$ using $N \times N \times N$ particles, either cubic or spherical, where red surfaces represent a large optical force aligned with that surface's normal (the XYZ directions), and blue being a large anti-aligned force. The mesh is at the edge of a Laguerre-Gaussian beam, which has been offset by $\mathbf{r} = [1.13 \times 10^{-6}, 0, 0]m$ for a clearer visualisation (the origin is given at the centre of the Laguerre-Gaussian beam).

By refining a cubic mesh (total half-width $R_m = 200nm$) with spherical and cubic particle primitives, as seen in figure 10, a numerically exact reference can be generated by considering a 1 particle, many dipole cubic mesh which will then be compared to the subdivided equivalents. Figure 11a shows the total force experienced by each mesh in a given setup and demonstrates that refining the dipole number results in convergence to some value which improves with reducing particle size (increas-

ing particle number). Importantly, however, these values for spherical primitives do not converge to the same value as the reference cube (unless 1 dipole per particle is used) as the total volume of dipoles is different, and so a strictly lower magnitude of scattering will be experienced no matter how refined the system is. Spikes are also observed as the dipole sizes do not divide exactly into the particle sizes, hence space has to be left (and so volume is further non-conservative). Figure 11b applies volume correction to each particle, which increases the radii of spherical particles by a factor of $\sqrt[3]{(6/\pi)}$ to ensure the volume with the spherical primitives matches the case with cubic primitives. Clearly this improves the accuracy of the model with sphere primitives, however it should be noted that again this does not agree exactly due to the particles needing to be shifted to avoid overlap and so, in a beam with a narrow high intensity annulus, still results in slightly differing convergence. Optimally, each dipole should experience a roughly constant field over its full volume, however an extreme case (like figure 9) better accentuates the difference when considering each model and the effect of volume conservation, demonstrating that for less sharp beam

profiles convergence is even easier to reach when modelling a system with spherical primitives.

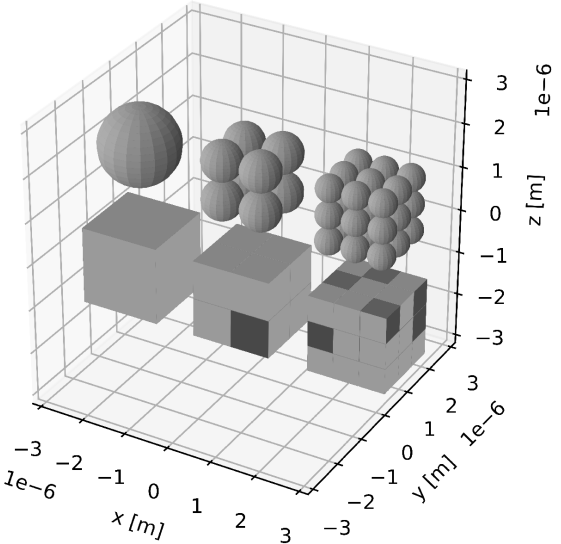
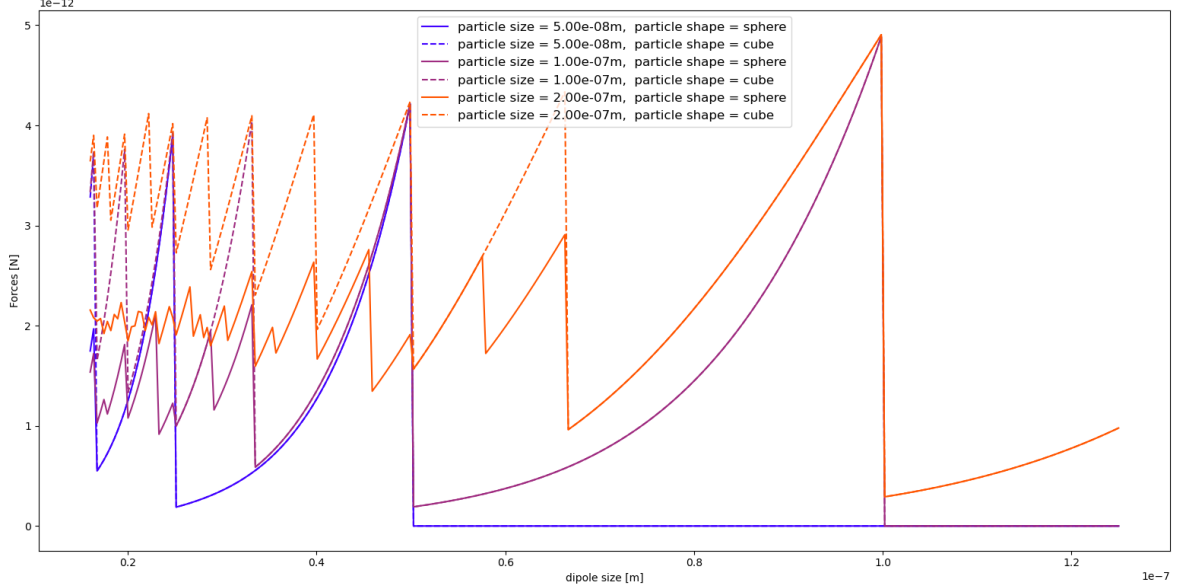
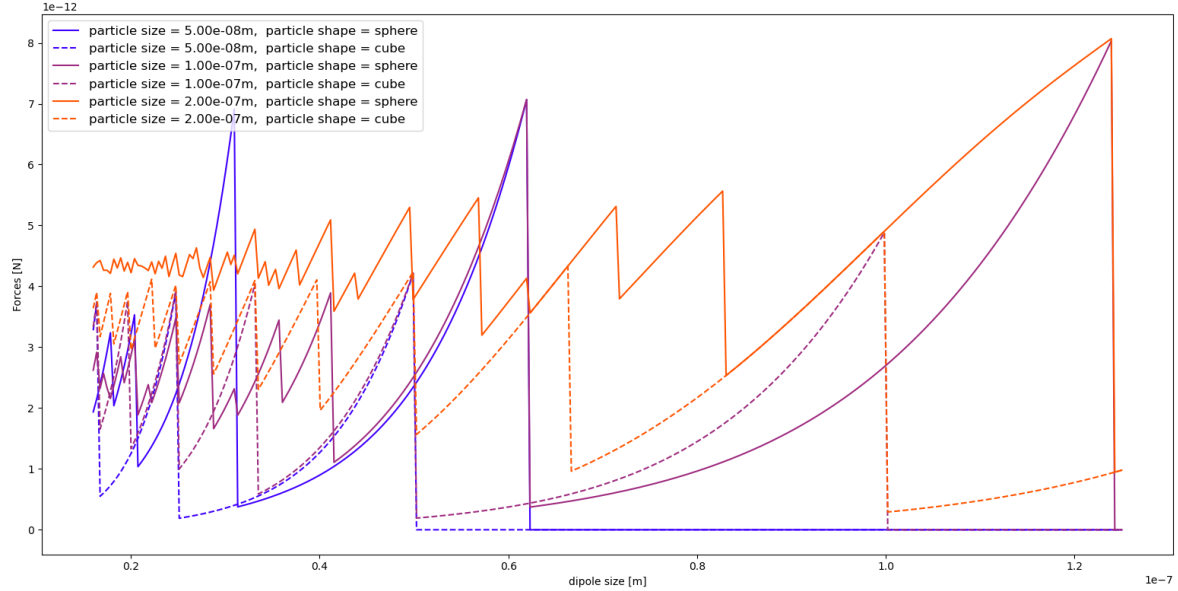


Figure 10: Examples of how meshes are refined by increasing the number of particles per mesh, where the spheres and cubes have equal radii and half-widths respectively (no volume correction). Considering volume correction would result in the radii of the spheres being larger (than the cubic half-widths) to match the total volume seen in the complete cubic mesh. As well as this, each particle seen can be further refined by increasing the number of dipoles used to model each (subdivisions of each particle seen).



(a)



(b)

Figure 11: The total optical force experienced by each mesh, as setup in figure 10 where the total mesh has a half-width $R_m = 200\text{nm}$, with (a) not accounting for volume differences in spherical and cubic primitive cases, and (b) including a volume correction. This correction will increase the spherical particle sizes, and so will exceed to the total width of the original mesh, but will maintain the same volume. ‘Particle size’ refers to the half width or radius of particles being considered. The dipole size varies along the X axis, particle size is varied through the colour and the primitive particles used are given by the line style.

3.3 Sphere and Torus Models

Following a similar line of thought to the previous experiment, the macroscopic properties of a known object will now be considered in a LG beam.

Considering the resulting motion will then inform

whether behaviour of this larger object (relative to its constituent particles modelling it) is correctly given by the simulation when purely optical forces are involved.

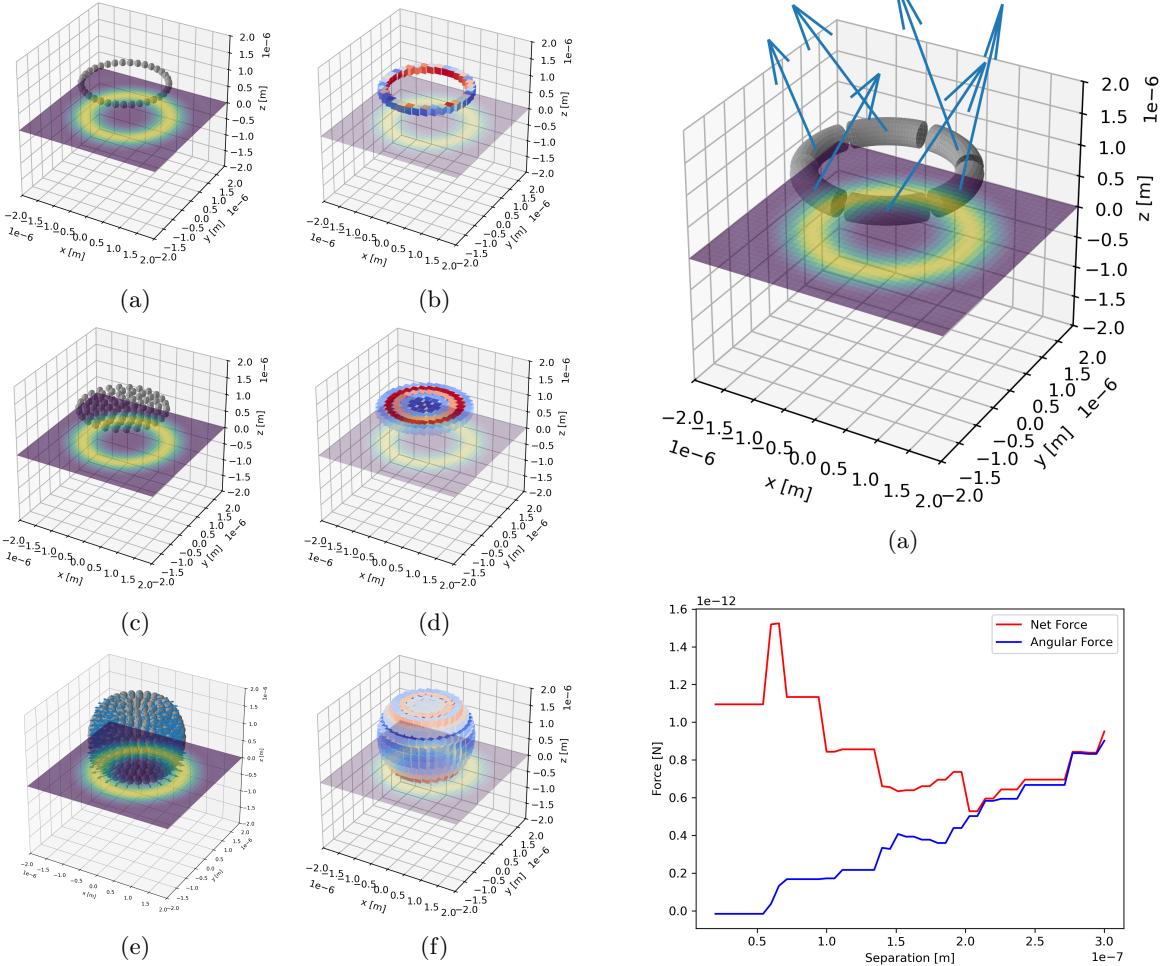


Figure 12: (a), (c), (e) show the transition between models used to achieve a final solid sphere model. (b), (d), (f) show the same transition, however also show the total optical forces through each axis displayed through the surfaces a cube being coloured (primitives are still spherical however), where red represents a large force along the normal direction, blue represents a large force in the opposite direction to the normal and white represents a small force. All setups are considered in a left circularly polarised Laguerre-Gaussian beam of order 3.

The rotational motion of an absorbing sphere in a Laguerre-Gaussian beam (figure 4) has been documented[29] and will be reproduced here through a set of tightly bound spheres, layered to form discs and stacked for a solid spherical setup. Extension to a non-absorbing material will also be considered too. Additionally, experimentation will be performed on torus segment primitives (as seen in figure 1b).

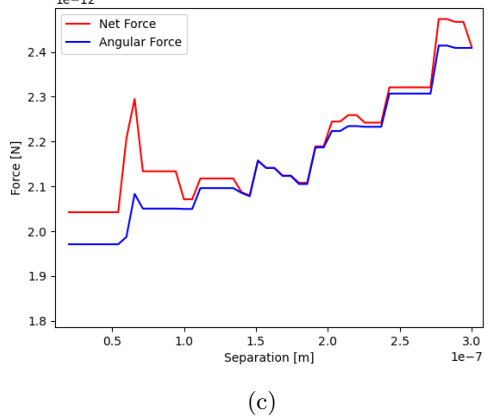


Figure 13: (a) shows the setup of 6 torus sectors with varying separation between each. Torus sectors equally fill up as much space as possible, leaving just the required total separation spread between all sectors. The arrows show the total optical force vector experienced by each sector. (b) and (c) show the averaged net and angular optical forces for each sector when the material of the sectors are non-absorbing ($n = 1.458 + 0i$) and absorbing ($n = 1.458 + 0.01i$) respectively. Torus primitives are used.

Figures 12a-12f have corresponding force data figure 14 for the net and angular force observed on a sphere of total radius $R_m = 1.5\mu m$ offset by $Z_h = 1\mu m$ in the Z axis (considered for the particle at $\mathbf{r} = [R_m, 0, Z_h]$). Separation here refers to the spacing between particles on a given concentric ring and not between each ring or stacked disc, and so it is observed that as the particles are brought close together in large collections for non-absorbing particles the angular force (hence torque on the sphere) tends to zero. Equally, for an absorbing material this tends towards a fixed value uniformly offset from the non-absorbing case, which matches the physical behaviour of a large particle trapped in a Laguerre-Gaussian beam [29], as experimentally a torque has been observed and concluded to be a result of material absorption, therefore no absorption implies no torque should be present, as observed. Let it also be noted that independently particles would, due to their radius of $R_p = 100nm$ in a beam of wavelength $\lambda = 1\mu m$, circularly orbit the high intensity annulus in both the absorbing and non-absorbing case due to the imparted orbital angular momentum. Therefore whilst the absorbing case of angular momentum may not be as surprising, the non-absorbing result that orbits actually cease is an interesting and crucial finding showing a strict change in behaviour from collective scattering, which is referred to as optical binding behaviour (a known symptom of optical scattering resulting in the correlated motion of scattering particles[30]). The data above also shows how the same effect is seen in both the disc and ring, indicating the bulk behaviour has a slight smoothing effect, however the surface drives the core behaviour. Note that the radial force component would be cancelled

in a solid bound material but the angular force would not.

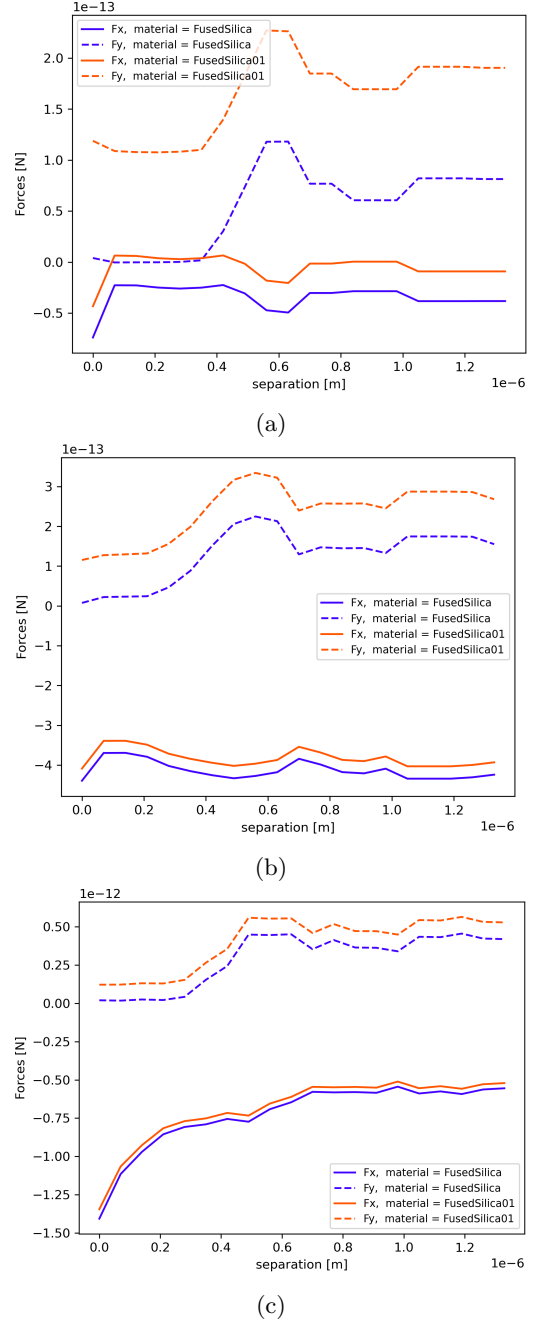


Figure 14: (a), (b) and (c) show the X and Y forces on a particle located at the edge of the mesh (corresponding to a radial and angular force respectively) for a ring, disc and sphere mesh (as in figure 12). For the ring and disc cases a particle radius $R_p = 100nm$ and dipole radius $R_d = 50nm$ is used, whereas the sphere case used $R_d = 100nm$. $F_{x,y}$ refers to the optical force in the given axial directions, and materials 'FusedSilica' and 'FusedSilica01' refer to materials with refractive index $n = 1.458 + 0i$ and $n = 1.458 + 0.01i$ respectively. Forces here are instantaneous and considered for a single frame.

Further consideration for the ring case, simulating the behaviour of a torus mesh, shows how the reduction of dipole size (standard DDA refinement) significantly improves this convergence to the true behaviour as seen in figure 15, as well as the same convergence seen when bringing a set of 6 torus primitives closer together (figure 13). Whilst a direct measurement of toroidal behaviour has not been observed the prior experiment showed agreement between the torus and sphere, and so this convergence would not be unexpected and would be ideal for further research to verify if this observation is true and whether this simulation is predictive of this.

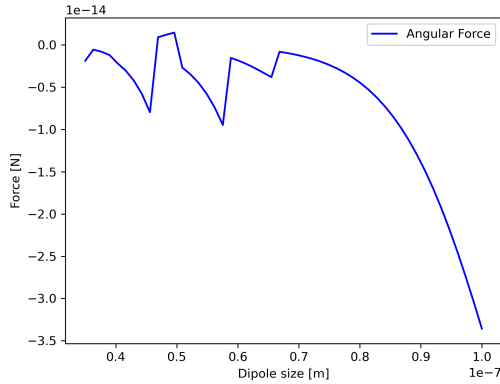


Figure 15: Optical force experienced by particles placed in a ring along a Laguerre-Gaussian high intensity annulus (as in figure 12a) as the dipole size is varied. Particles are taken to have radius $R_p = 200\text{nm}$ and dipole radius $R_d = 40\text{nm}$ with 16 total spherical particles inside the ring (filled ring). Just the angular component of force averaged across all particles is considered.

4 Experimental Application

Now that verifiable meshes have been observed to be optically well approximated by a series of closely packed and refined spherical particle primitives this section will consider the effect of these meshes but with the full set of required forces (from particle connections too) needed to dynamically step the

particles in a mesh, to satisfy the project’s second aim, as opposed to just considering single frame behaviour as has been done up to this point. The term ‘structural parameters’ will refer to the spring and bending coefficients k_{spring} and $k_{bending}$ respectively, which dictate magnitudes of the spring and bending forces on connected particles.

4.1 Rod Deformation Models

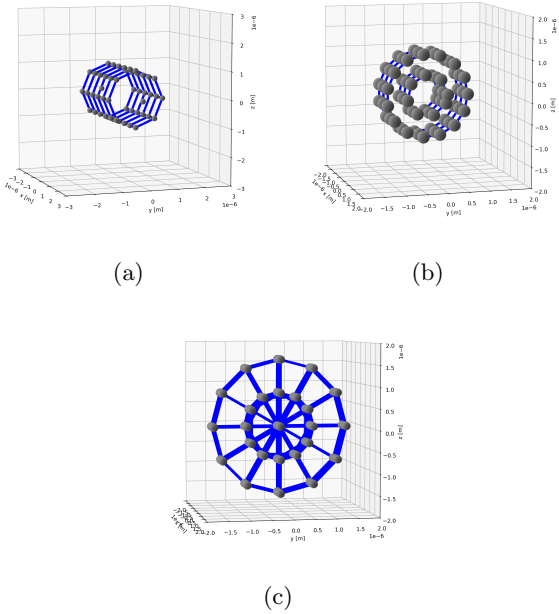


Figure 16: Depicts example model cross-sections to be considered for a flexible micro-rod simulation. The blue lines between particles represent a connection, allowing spring and bending forces to be transmitted. The hollow, layered and uniformly connected models are intended to model empty, partially filled and solid materials respectively.

By considering micro-rods with silica beads attached to either end, deflection was experimentally induced when one bead was optically trapped in place while the other translated along the axis separating them (using translating optical tweezers), resulting in buckling[31]. Here a similar setup will be considered however the trapping Gaussian beams will now both be circularly translating, as seen in

figure 17. Such a translation should ease the rod into its deflection in opposition to simply compressing the rod (which within a simulation can result in stability problems with particle separation before any buckling has time to occur). Note however that to achieve an entirely accurate result, the complex structure of a specific material would have to be approximated by the model 16, and so we would expect different models to work for each material, for instance a particle constructed from axial fibres would require anisotropic spring and bending coefficients (constants allowed to vary throughout the material) to replicate this detailed structural difference, however the ultimate goal here is to assess whether this range of motion is possible to be achieved through a bead and spring framework, so structural parameters could be mapped to any specific value through some separate tuning means.

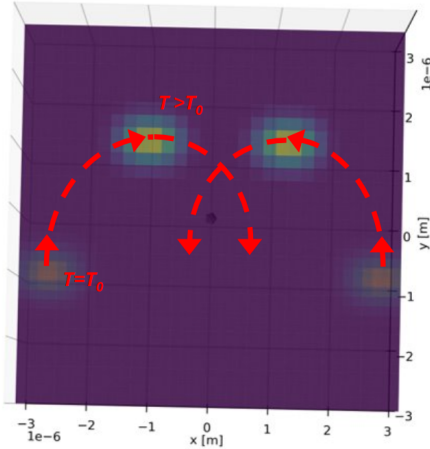


Figure 17: Two Gaussian beams translating circularly over time (shown through the shaded and default beam brightnesses), performed to slowly induce deflection in the rod and avoid unstable buckling. This motion occurred between angles $\theta = [0, \pi/2]$, and was taken to occur slowly (over the course of 90 frames). A time step of $dt = 1.25 \times 10^{-5}s$ was used for all rod dynamics simulations.

Qualitatively figures 19b and 19a demonstrate the

motion ranges found using a hollow rod model (figure 16a) when inducing a deflection. Therefore it can be seen that choosing a large $k_{bending}$ alongside a large k_{spring} will result in very strong deformation that will often break free from the optical trap, but a reduced spring constant will give a greater deflection as less particles are forced to move up with the trap (figure 19b). Equally, for low $k_{bending}$ we can generate a continuum of gentle deflections by varying k_{spring} (figure 19a). Hence a full spread of deflections can be found through the tuning of just these two structural parameters when dealing with a hollow shell model.

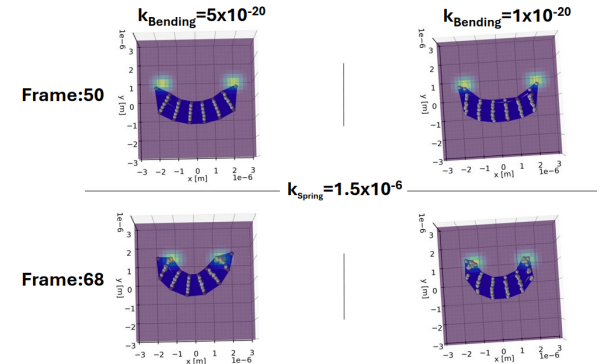


Figure 18: Deformation of a uniformly connected rod model (8 particles across its length, 6 particles angularly and 2 layers with a central fibre considered) using varying parameters after the system has been allowed to evolve. Translated Gaussian beams trap (as in figure 17) the silica bead particles on either end of the rod, with refractive index $n = 1.458 + 0i$, and the particles have $n = 1.41 + 0i$. Connections are shown through blue lines joining relevant particles. A spring constant of $k_{spring} = 1.5 \times 10^{-6}$ is used for all experiments here.

As well as this, figure 18 demonstrates deformation for a uniformly connected model (figure 16c), which exhibits similar levels of deflection to the hollow rod despite having a much smaller $k_{bending}$ constant (for a similar k_{spring} too), due to the 50% increase in connection number and additional particles intro-

duced (in the bulk volume). These give rise to noticeably larger forces involved, but can still be tuned for reasonable deformation, as observed, whilst accounting for optically interacting mass that was previously neglected. When considering a model such as 16b, designed to give volume scattering without additional connection forces, unstable behaviour is immediately seen due to dynamics quickly resulting in overlapping particles and hence invalid forces.

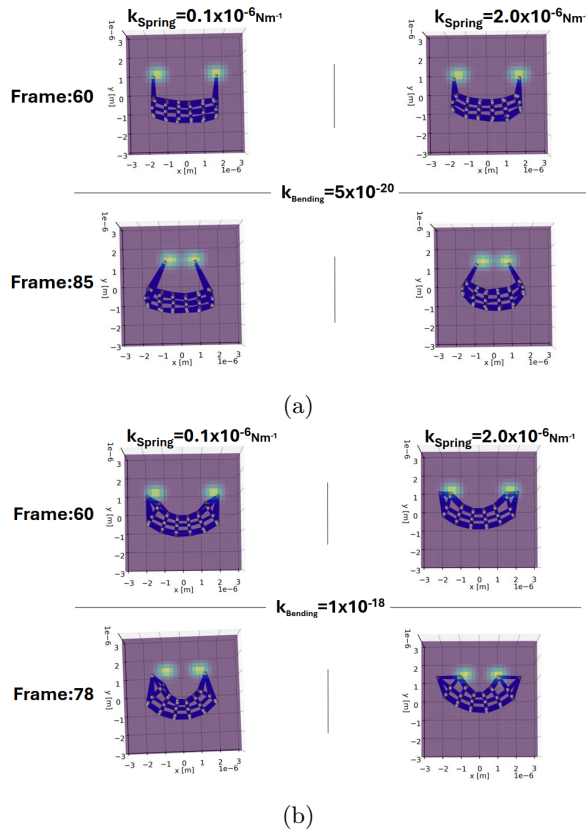


Figure 19: Deformation of a hollow rod model (8 particles across its length, 6 particles angularly) using varying parameters after the system has been allowed to evolve. Translated Gaussian beams trap (as in figure 17) the silica bead particles on either end of the rod, with refractive index $n = 1.458 + 0i$, and the particles have $n = 1.41 + 0i$. Connections are shown through blue lines joining relevant particles. Different frames of evolution are considered here as motion became unstable before frame 85 in some experiments run (due to stronger interactions from larger constants used). Two separate bending constants, $k_{bending} = 5 \times 10^{-20}$ and $k_{bending} = 1 \times 10^{-18}$, are considered here alongside varying spring constants k_{spring} .

This could be corrected with a better scaled implementation of the Buckingham force, however would require more careful tuning to achieve a stable system. It should also be considered that due to the greater number of connections with the bead (compared to the hollow model) the stiffness constant between the beads and outer end surfaces of the rod had to be smaller to prevent unstable motion occurring in these later examples.

4.2 Optical Stretchers

Osmotically swollen RBCs have been experimentally stretched within an optical stretcher setup (where varying beam foci offsets, Z_{focus} , can be considered as in figure 20) of varying powers[32]. Simulating these cells as meshes is ideal since they can be, when swollen with water, modelled as hollow spherical membranes since the simulation assumes particles are immersed in a medium of refractive index $n_{medium} = 1.33$. The refractive index of each particle can be taken to be $n_{particle} = 1.41 + 0i$ to model the mesh as a RBC. Therefore to verify the performance of the simulation it must be ensured that the volume of the cell is conservative when stretched, as we would expect a Poisson ratio $\nu = 0.5$ for biological membranes[32], implying incompressibility[33]. Equally, the shape of the deformation should be measured to ascertain whether the stretched cell has reasonable properties (such as polar symmetry for a stretcher in the Z axis) and for experimental comparisons.

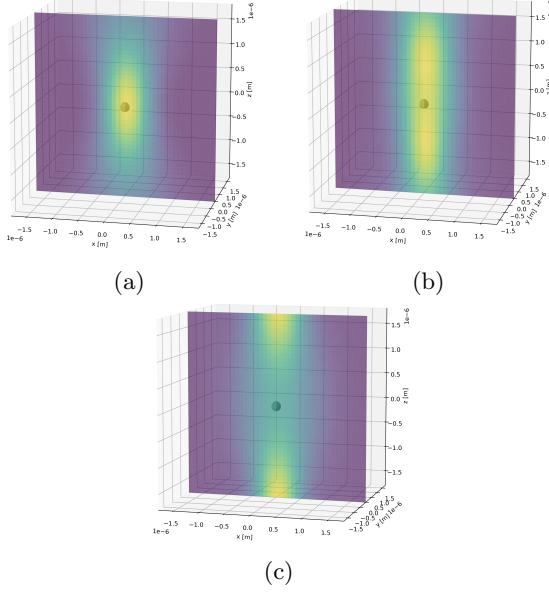


Figure 20: The field intensity is plotted for a set of counter-propagating X and Y polarised Gaussian beams, propagating in the Z and negative Z axes. Their foci are offset by $0\mu m$, $1\mu m$ and $2\mu m$ along their propagation direction, respectively for figures (a)–(c). The focus of both beams can be observed to shift here.

A spherical membrane can be generated by placing particles evenly across its surface with connections to the nearest N neighbouring particles[34] ($N = 5$ for all experiments run here). Setting the power of the optical stretcher, $P = 110mW$, wavelength $\lambda = 0.785 \times 10^{-6}m$ and beam width $w_0 = 2.7\mu m$ (hence implying a beam strength $E_0 = 2.7 \times 10^6 NC^{-1}$, from equation 11) allows experimental comparison to the results of figure 22[32]. Apply the dynamics simulation to this set of connected particles, with a total mesh radius of $R_m = 3.36\mu m$, for varying k_{spring} and $k_{bending}$ constants will allow the parameters that are required for a RBC model to be found by considering the height-to-width ratio (HWR) achieved by the simulation, which is the ratio of Z width, W_z , and averaged X and Y widths $W_{xy} = \sqrt{W_x W_y}$ such that $HWR = W_z/W_{xy}$, where these widths are found using the bounding box of

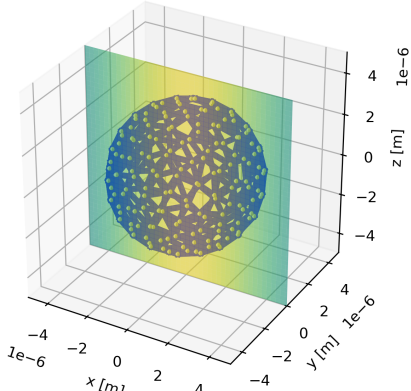
the mesh (which will introduce some inaccuracy if the mesh rotates). Enclosed mesh volumes can also be calculated through usage of the Python method *ConvexHull*[35], which approximates the bounding mesh for the set of particle positions given and calculates the total volume by summing tetrahedral sub-volumes formed with the origin, therefore assuming the mesh is non-concave which will be true for all meshes tested (given small deformations are considered). The moment of inertia (MOI) of the mesh can simply be found using the analytical expression

$$\mathbf{I}_j = \sum_{i=1}^N m \mathbf{r}_{i,j}^2, \quad (14)$$

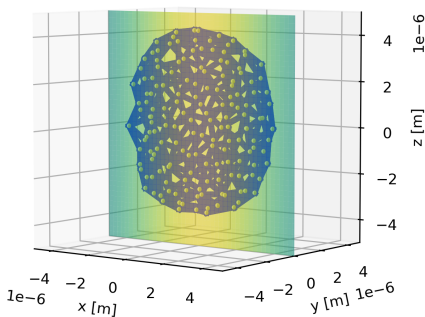
where m is the mass of each particle within the mesh, $\mathbf{r}_{i,j}$ is the j^{th} position component of the i^{th} particle and \mathbf{I}_j is the j^{th} component of the MOI for the mesh. For an ideal ellipsoid you can simply find this using[36]

$$I_{ideal} = \frac{1}{3} M(a_1^2 + a_2^2), \quad (15)$$

such that M is the total mass of the mesh and $a_{1,2}$ are the semi-axes perpendicular to the MOI component being measured. Comparing these calculated values will allow evaluation of whether the resulting deformation is ellipsoidal, and if not will hint at the distribution of particles.



(a)



(b)

Figure 21: Depicts the initial and evolved shape of the mesh. Spherical particle primitives (200 used) are placed evenly about the surface of a sphere[34] and connected to the nearest 5 neighbouring particles, with 1 dipole per particle. Optical, spring and bending forces are considered during dynamics. This evolved mesh shown has an approximate height-to-width ratio HWR = 1.5 (as a diverging example). The Gaussian foci are offset to $Z_{focus} = \pm 50\mu m$, with beam width $w_0 = 2.7\mu m$, wavelength $\lambda = 0.785 \times 10^{-6}m$ and $E_0 = 2.7 \times 10^6 NC^{-1}$. It is also taken that each particle and dipole has radius $R_p = R_d = 100nm$ with a total mesh radius $R_m = 3.36 \times 10^{-6}m$ and a time-step $dt = 1 \times 10^{-4}s$ is used. These parameters will be used in all experiments except where specified otherwise.

Setting up a simulation as described in figures 21 and 24 (parameters given in the figures), it is seen that each configuration is repeated 3 times due to the random Brownian motion component included in the dynamics which gives rise to different curves when evolved, however each still demonstrates the same behaviour, such as the convergence

to $HWR \approx 1.31$ in figure 24a. Experimentally for equivalent parameters $HWR \approx 1.34$ (figure 22) has been observed, which is in very close agreement for this choice of k_{spring} , $k_{bending}$.

Such convergence is also affected by the number of particles, $N_{particles}$, modelling the system (seen when comparing to figure 25a) where a system of greater particle refinement has already been shown to more accurately converge to the desired model's behaviour (sections 3.2-3.3). Equally, the figures 24a and 26a show how a change of structural parameters allow the convergent HWR to be selected (just as any material of arbitrary elasticity may deform to differing degrees within an optical stretcher), and so figure 24 gives a more valid result than its $N_{particles} = 100$ counterpart, but may be further refined with more particles. This would result in slightly different structural parameters (which eventually converge to their true value) at the cost of significantly higher computational time, hence a reasonable parameter set has been given with this in mind.

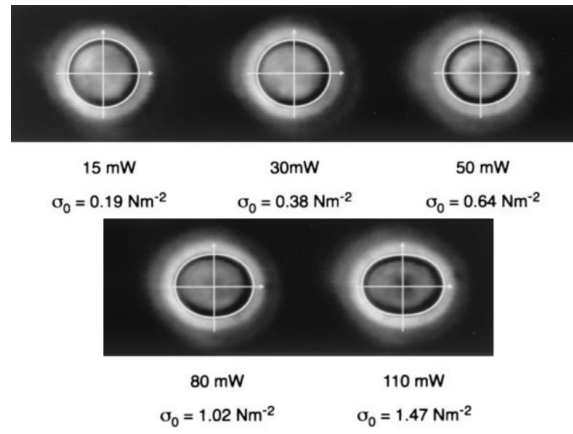


Figure 22: Figure reproduced: Guck, Jochen, et al. "The optical stretcher: a novel laser tool to micro-manipulate cells." Biophysical journal 81.2 (2001): 767-784. Depicts experimental results for osmotically swollen red blood cells in an optical stretcher setup at different powers, P , where for $P = 110mW$ a height-to-width ratio $HWR \approx 1.34$ is found.

Therefore by tuning the bead and spring model (purely material properties, not the system it is within) you are able to achieve many degrees of flexibility, meaning that in theory any specific material (anisotropic included, however this has not been considered here) can have a spring and bending coefficient matrix determined to generate the requisite action for each connection, giving one of these known to exist ranges of motion, as hoped.

Verifying whether the deformed shapes are physically feasible, when stable shapes are found (convergent HWR) the corresponding volumes are considered (figures 24b and 25b) to see if the volume becomes stable as well. As an average, this can be difficult to determine as the figures carry significant noise, due to sensitivity of the volume to single unstable particles which suddenly jump (as the volume is found from the bounding mesh), however we see for individual repeats that volumes do also converge when HWR converges (for example, most clearly in figure 23b for times $t > 0.3s$, or in figure 25 considering repeat 2 for $t > 0.2s$). A consistent pattern across all figures is the initial sharp jump in volume, which then gradually declines up to the time convergence begins, where final values as a fraction of their original volume ($V_0 = 1.56 \times 10^{-16} m^3$) are approximately 0.93, 0.82 and 0.95 for figures 24b, 25b and 23b respectively (using the average final volume of repeats which converged for each). Taking an average for the diverging case, figure 26b, gives an approximate ratio of 1.04, however the repeats for cases like this show significantly greater variation in final volumes (since convergence is not required). Therefore these volumes on average show good agreement with the volume conservation re-

quired, and for longer evolutions such as figure 23 only show variations in the volume difference between -8% and $+1\%$, which is similarly seen for the other converging cases (however, this assumes the simulation has had sufficient time to evolve and stabilise).

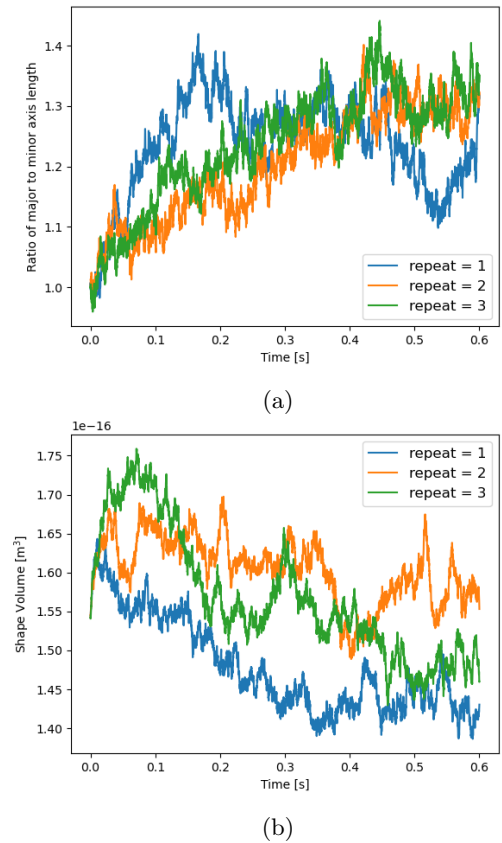


Figure 23: The height-to-width ratio, total volume and moment of inertia plots for a spherical mesh using stable parameters. Parameters used follow figure 21, but with spring and bending constants $k_{spring} = 0.46 \times 10^{-7} Nm^{-1}$, $k_{bending} = 1.38 \times 10^{-20}$. This simulation was run for 6000 frames per repeat at a time-step $dt = 1 \times 10^{-4}s$.

Investigating the MOI for all simulations reveals an offset in the each of the X, Y and Z axes, however crucially the curvature observed in each analytical calculation, that is using equation 14 directly, quite closely resembles the corresponding behaviour for an ellipsoidal ensemble, considering the perpendicular semi-axes, found using equation 15. An immediate reason for why this may be the

case is due to the bounding box measure used for the ellipsoidal version giving semi-axes which are significantly impacted by single particles suddenly jumping, a consequence of simulating many particles that are closely packed (notice that the regions in which the MOI gradients do not match strongly is for lower times where a jumping HWR was found, also using bounding box calculations). Therefore this offset is likely largely a consequence of this calculation, which could be accounted for by averaging the number of particles required for the bounding box tolerance, however this would result in a noticeable initial MOI reduction (unless much larger par-

ticle numbers were used). Considering this in addition to the small gradient differences across later time intervals and a consistent under-valuation of the analytical MOI relative to the ellipsoid suggest the simulated deformation is more concentrated towards the Z axis (a smaller offset between the Z compared to X and Y components of MOI is seen in all figures, particularly towards the final time where convergence has occurred), with a closer match to an ellipsoid in the X-Y plane. This qualitatively suggests the simulation deformation is less ellipsoidal, but is rather a version more compressed by some small factor to bring particles closer to the Z axis, maintaining a correct profile in the X-Y plane.

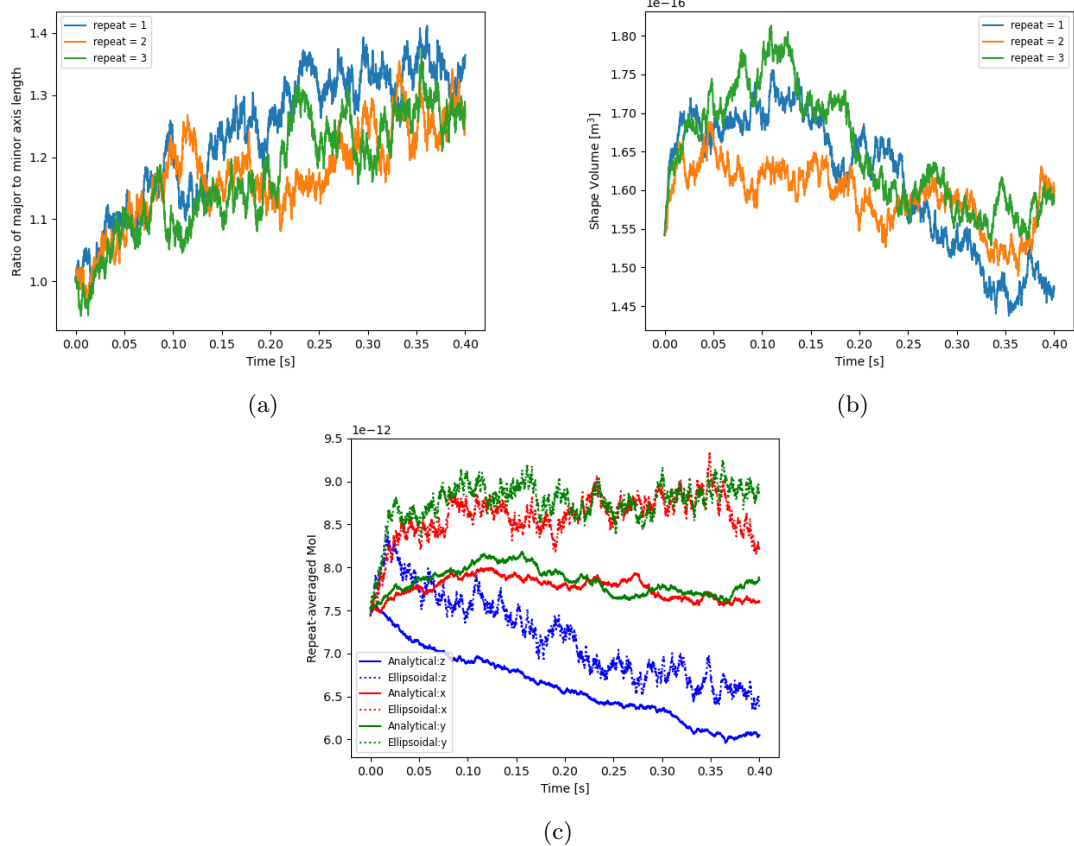


Figure 24: The height-to-width ratio, total volume and moment of inertia plots for a spherical mesh using stable parameters. The moment of inertias (MOI) compared here assume a mass $m = 1\text{kg}$ per particle for simplicity as only the comparisons in behaviour are considered. 'Analytical' refers to the simulated MOI using equation 14, and 'Ellipsoid' refers to the assumed elliptical MOI using equation 15 with semi-axes taken from the bounding box of the mesh. Parameters used follow figure 21, but with spring and bending constants $k_{\text{spring}} = 0.42 \times 10^{-7} \text{Nm}^{-1}$, $k_{\text{bending}} = 1.25 \times 10^{-20}$, and a particle number $N_{\text{particles}} = 200$. This simulation was run for 4000 frames per repeat at a time-step $dt = 1 \times 10^{-4}\text{s}$.

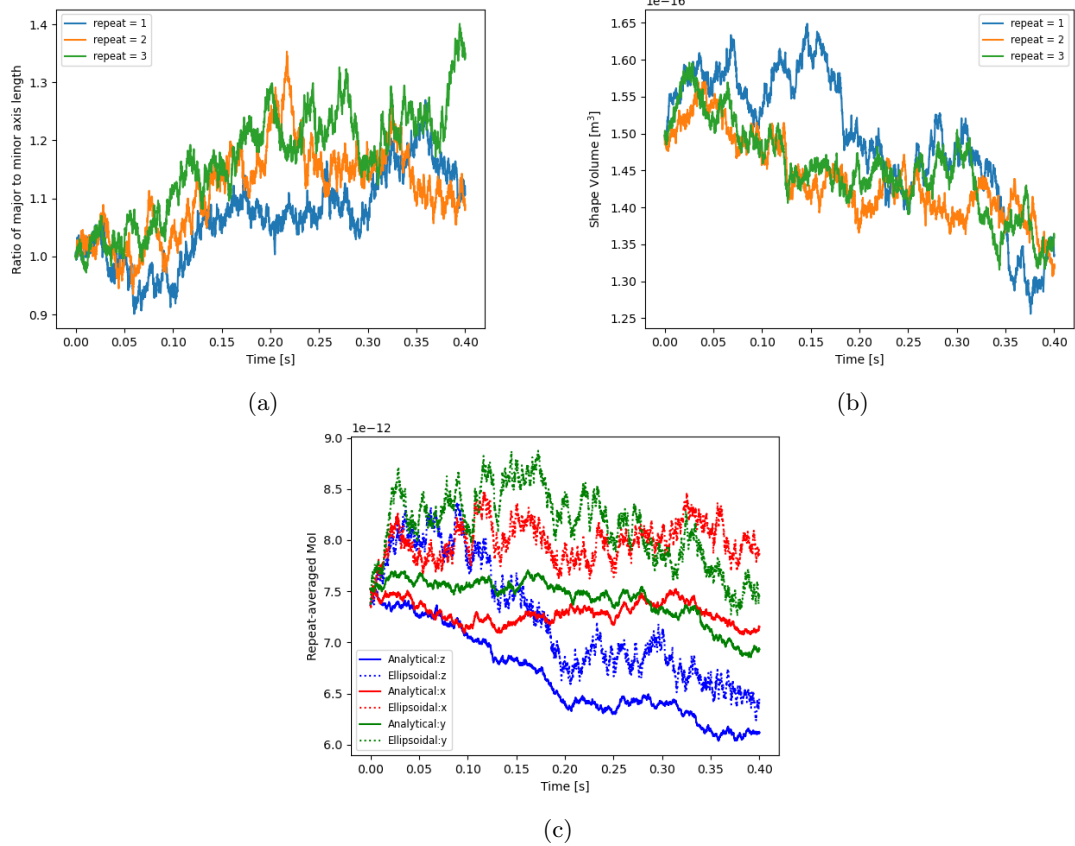


Figure 25: The height-to-width ratio, total volume and moment of inertia plots for a spherical mesh using stable parameters. Parameters used follow figure 21, but with spring and bending constants $k_{spring} = 0.42 \times 10^{-7} Nm^{-1}$, $k_{bending} = 1.25 \times 10^{-20}$, and a particle number $N_{particles} = 100$. This simulation was run for 4000 frames per repeat at a time-step $dt = 1 \times 10^{-4}s$.

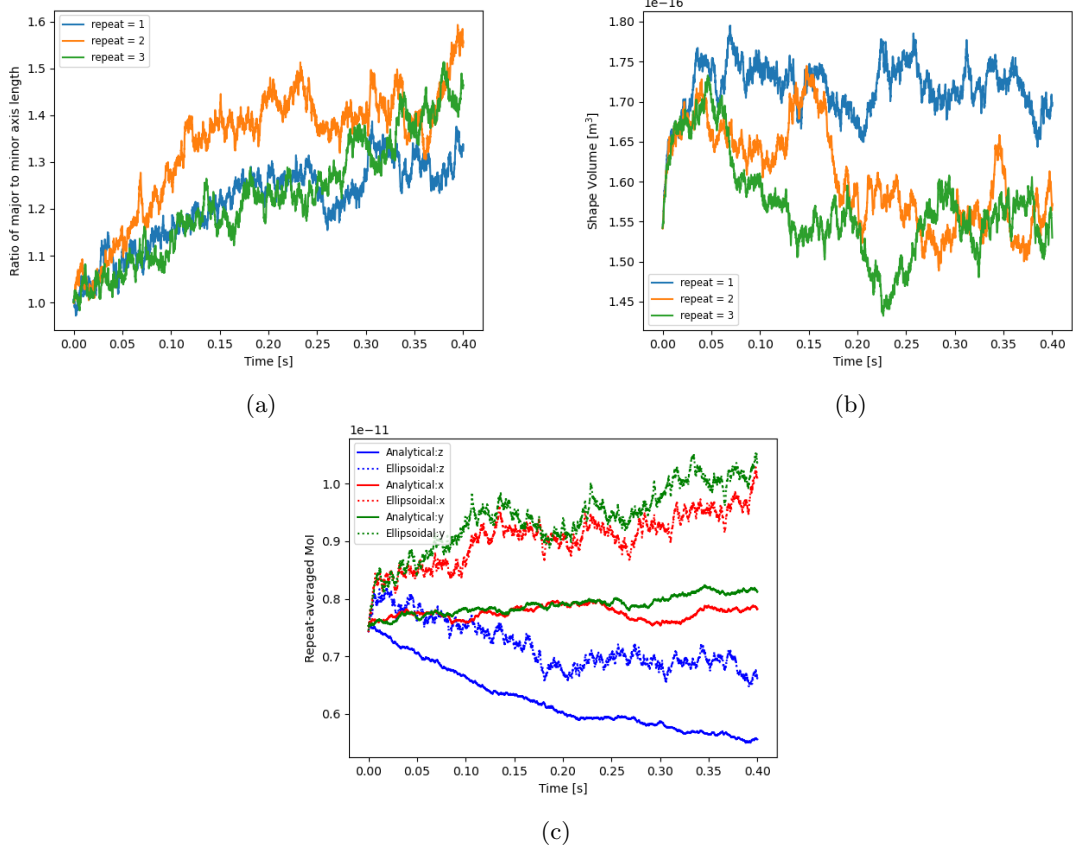
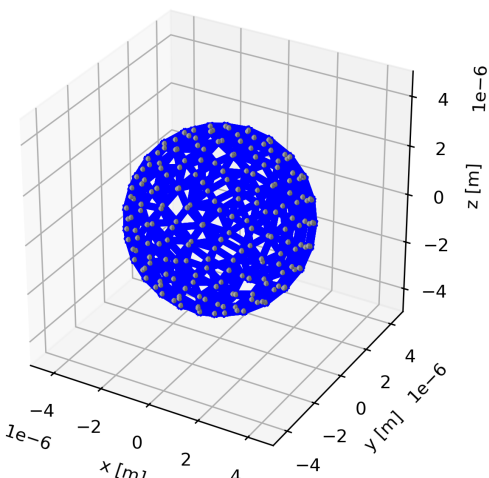


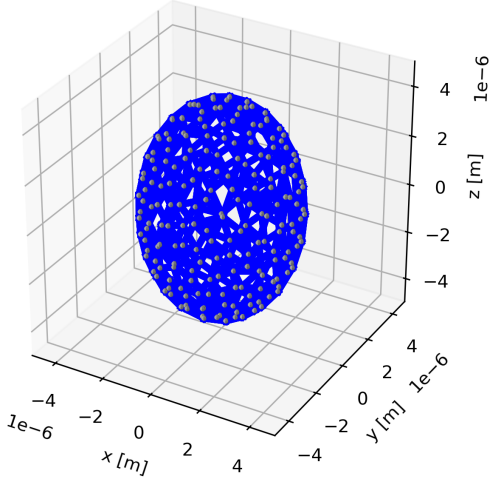
Figure 26: The height-to-width ratio, total volume and moment of inertia plots for a spherical mesh using unstable parameters. Parameters used follow figure 21, but with spring and bending constants $k_{spring} = 0.25 \times 10^{-7} Nm^{-1}$, $k_{bending} = 0.75 \times 10^{-20}$, and a particle number $N_{particles} = 200$. This simulation was run for 4000 frames per repeat at a time-step $dt = 1 \times 10^{-4}s$.

To further investigate the shape which the dynamics converged to, a transformation was applied directly to the initial mesh setup (no dynamics performed) and the force in each octant (formed from the axial planes) was measured. By considering where all the forces equal zero it can be concluded that it is feasible a mesh in this setup can be stable (however individual particle motion may still de-stabilise the octants), but if this condition is not met the transformed mesh cannot possibly be stable (immediately wants to separate). Applying this approach, figure 28c demonstrates how an analytically volume-conserving linearly stretched spherical shell (as in figure 27) can find a stable HWR for very high structural parameters, hence a tightly constrained system essentially to the original shell shape. How-

ever, when reducing the constraints for such a system (figure 28a) since volume conservation stretches the Z more than the X or Y axes individually, the Z scaling occurs too quickly meaning the X,Y and Z components will not simultaneously have zero force for a reasonable ($HWR = 1.34$ for $P = 110mW$) stretching factor. Considering the same structural parameters as was shown to be stable above in figure 24, figure 28b also shows that specifically linear stretching will not result in a potentially stable state with these parameters. This eliminates a simple linear scaling, volume-conserving transformation for the true deformation experienced by a sphere membrane in an optical stretcher like this, as was seen in the dynamics simulation too.

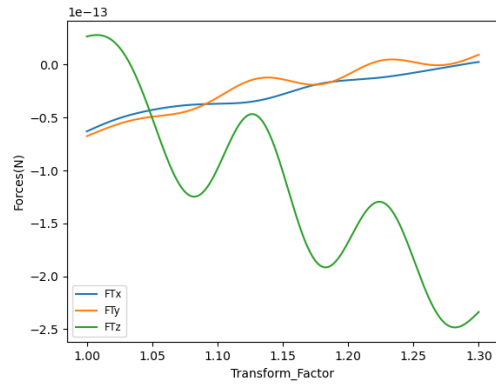


(a)

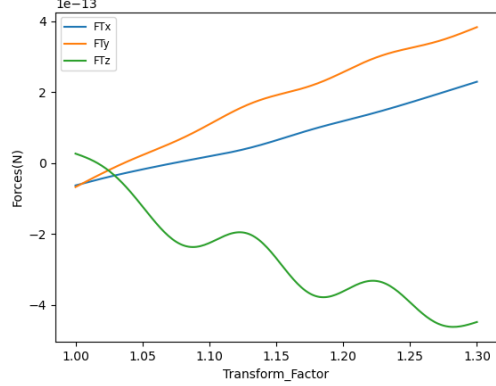


(b)

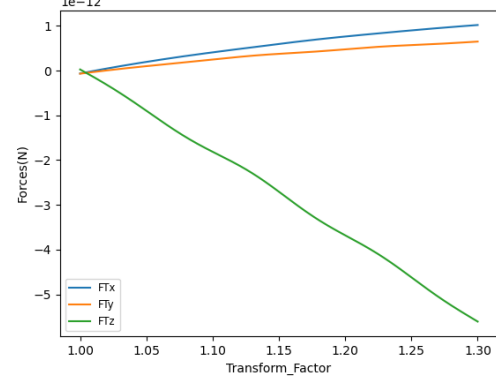
Figure 27: Depicts the transformation generated manually on a set of particles on a spherical membrane. A volume-conserving linear transformation is applied to the points, stretching them along the Z axis and compressing them equally along the X and Y axes. For a given transform factor (Z stretch ratio) a height-to-width ratio for the full mesh can be found. Particles have their Z coordinate stretched by the transform factor, and the X and Y coordinates compressed by the square root of the transform factor, hence $V = (4\pi/3)(a_1 a_2 a_3 \times T \times T^{-1/2} \times T^{-1/2}) = (4\pi/3)(a_1 a_2 a_3)$ is conserved.



(a)



(b)



(c)

Figure 28: Forces experienced by each octant when using low, dynamically stable and high structural parameters, being $k_{spring} = 0.1 \times 10^{-7} Nm^{-1}$, $k_{bending} = 0.1 \times 10^{-20}$ for (a), $k_{spring} = 0.42 \times 10^{-7} Nm^{-1}$, $k_{bending} = 1.25 \times 10^{-20}$ for (b) and $k_{spring} = 1 \times 10^{-7} Nm^{-1}$, $k_{bending} = 5 \times 10^{-20}$ for (c). FTx, y, z corresponds to the total (optical, spring and bending) forces in the XYZ directions. The spherical mesh has radius $R_m = 3.36 \times 10^{-6} m$, particle and dipole radii $R_p = R_d = 100 nm$, beam field strength $E_0 = 2.7 \times 10^6 NC^{-1}$, beam width $w_0 = 2.7 \mu m$, particles used $N_{particles} = 200$, wavelength $\lambda = 0.785 \times 10^{-6} m$ and foci separation $Z_{focus} = \pm 50 \mu m$.

5 Conclusions

Current techniques for simulating the dynamics of a deformable body without optical interactions have existed for decades and provided a strong framework in molecular simulations, but have not been shown to apply when light scattering is critical to the system's behaviour. Here, the bead and spring model was validated with DDA light scattering calculations to give optically accurate behaviour for a series of notable scenarios in which issues may arise, where larger meshes were modelled through simple primitive particles that each have known behaviour, crucially showing there existed distinct behaviour for the collectively modelled mesh in comparison to its individual constituents. The model had considerable performance improvements when its volume matched the target object's, hence research into irregularly shaped dipoles (accounted for by scaled polarisabilities) may yield better volume filling, and so better model accuracy.

Extending the model to micro-rods experiencing spring and bending forces demonstrated that a variety of flexibilities were able to be found by tuning structural constants (k_{spring} , $k_{bending}$), and so a model could be generated for some arbitrary complex structure through a choice of these parameters and connection configurations. When considering the experimental stretching observed for osmotically swollen RBCs the simulated dynamics were seen to converge to experimental values, with only small reductions in volume, after finding valid structural parameters alongside the specific beam parameters provided. The moment of inertia of this stable mesh was used to ascertain the general shape which an optically stretched cell tended towards, confirmed by experimental work.

Currently, the k_{spring} and $k_{bending}$ parameters have been shown to allow a variety of behaviours to occur, which was the aim of the project, hence to study real materials the selection of these constants would require either tuning of parameters through comparison to known deformation properties, or require a more sophisticated procedure to convert the structural qualities of a material into matrices of unique spring and bending coefficients to better apply the model. Once performed, this would allow the dynamics any material with arbitrary shape to be modelled flexibly and have group or solitary behaviours be measured for more accessible and affordable research that would ordinarily require a precisely tuned optical trap.

6 Appendices

Appendix A - LDR

Equation for the lattice dispersion relation (LDR) polarisability given by [9]

$$\alpha_{LDR} = \frac{\alpha_{cm}}{1 - (\frac{\alpha_{cm}}{d^3})[(b_1 + b_2 n^2 + b_3 n^2 S)(kd)^2 + (\frac{2}{3})i(kd)^3]},$$

$$S = \sum_i (\mathbf{a}_i \cdot \mathbf{e}_i)^2,$$

$$b_1 \approx 1.8915316,$$

$$b_2 \approx -0.1648469,$$

$$b_3 \approx 1.7700004,$$
(16)

where α_{cm} is the Clausius-Mossotti relation, \mathbf{a}_i and \mathbf{e}_i are the beam propagation and polarisation directions respectively, d is the diameter of a dipole/lattice spacing and k is the wave number.

Appendix B - ADDA

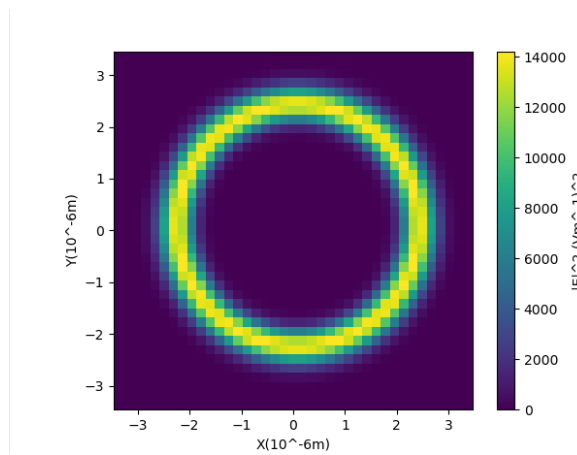


Figure 29: Intensity plot for an order 8 Laguerre-Gaussian beam. The field intensity calculations were performed in ADDA using a custom beam implementation, and the resulting data was displayed in Python.

ADDA is open source DDA software, which can be found at ScattPort[16] or on their GitHub page[37]. Work has been performed to setup Python scripts which generated geometry for each frame of a dynamics simulation using ADDA's multi-particle system. However, this required particles to be placed on a consistent lattice resulting in less freedom in particle placement. Additionally, forces could only be calculated for plane waves and so development had begun to separately perform these force calculations in Python using polarisation data generated by ADDA, however this was not completed. Our experimental work also wanted to consider Laguerre-Gaussian beams but these are not included in ADDA by default, and so were implemented (see figure 29) before work with ADDA stopped shortly after. The relevant files mentioned here can be found on my GitHub repository[38] (as a disclaimer the compiled copy of ADDA which I modified can be found here, however I did not develop ADDA, my only addition to this code was the inclusion of the Laguerre-Gaussian beam and

nothing else).

Appendix C - Buckingham Potential

The equation for the Buckingham potential and force implemented in the DDA dynamics software used[39][40], however the Buckingham force was not included for any final results due to the extreme compactness of particles often leading to an unstable result when paired with the Buckingham repulsion. The Buckingham potential is given by

$$V_{ij}(r_{ij}) = A_{ij} \exp\left(-\frac{r_{ij}}{\rho}\right) - B_{ij} r_{ij}^{-6}, \quad (17)$$

and hence the force can be found from this by taking the negative differential;

$$\mathbf{F}_{k,ij} = -[C_1 C_2 \exp(-C_2 r_{ij}) - \frac{32 H R^6}{3 r^3 (r^2 - 4 R^2)^2}] \frac{\mathbf{r}_k}{r_{ij}}, \quad (18)$$

with arbitrary constants A_{ij} , ρ , B_{ij} , and the specific constants implemented as $C_1 = 10^{-11}$, $C_2 = 0.4 \times 10^8$, $H = 1.2 \times 10^{-19}$.

Appendix D - MST

Maxwell's stress tensor (MST) calculation given by[41]

$$\begin{aligned} \mathbf{F} &= \int_S \langle \bar{\mathbf{T}}_M \rangle \cdot d\mathbf{S}, \\ \langle \bar{\mathbf{T}}_M \rangle &= \frac{1}{2} \operatorname{Re}(\epsilon \mathbf{E} \otimes \mathbf{E}^* + \mu \mathbf{H} \otimes \mathbf{H}^* - \frac{1}{2} [\epsilon |\mathbf{E}|^2 + \mu |\mathbf{H}|^2] \bar{\mathbf{I}}), \end{aligned} \quad (19)$$

where \mathbf{E} and \mathbf{H} are the electric and magnetic fields, $d\mathbf{S}$ is a surface area element and ϵ and μ are the permittivity and permeability for a material. This can be used to derive the force calculations 5 and 6 defined above, and was also applied directly in some earlier experimentation.

References

- [1] Arthur Ashkin, James M Dziedzic, John E Bjorkholm, and Steven Chu. “Observation of a single-beam gradient force optical trap for dielectric particles”. In: *Optics letters* 11.5 (1986), pp. 288–290.
- [2] Ruixue Zhu, Tatiana Avsievich, Alexey Popov, and Igor Meglinski. “Optical tweezers in studies of red blood cells”. In: *Cells* 9.3 (2020), p. 545.
- [3] Michelle D Wang et al. “Stretching DNA with optical tweezers”. In: *Biophysical journal* 72.3 (1997), pp. 1335–1346.
- [4] Osku Kemppinen et al. “Computational light scattering by atmospheric dust particles”. In: (2016).
- [5] Darya Yu Orlova, Maxim A Yurkin, Alfons G Hoekstra, and Valeri P Maltsev. “Light scattering by neutrophils: model, simulation, and experiment”. In: *Journal of Biomedical Optics* 13.5 (2008), pp. 054057–054057.
- [6] Ynon Hefets and Carynelisa Haspel. “Flexible scattering order formulation of the discrete dipole approximation”. In: *Applied Optics* 62.23 (2023), pp. 6093–6105.
- [7] YL Siu, Jones TK Wan, and KW Yu. “Computer simulations of electrorheological fluids in the dipole-induced dipole model”. In: *Physical Review E* 64.5 (2001), p. 051506.
- [8] Lei Li, Ronald G Larson, and Tam Sridhar. “Brownian dynamics simulations of dilute polystyrene solutions”. In: *Journal of rheology* 44.2 (2000), pp. 291–322.
- [9] Maxim A Yurkin and Alfons G Hoekstra. *User manual for the discrete dipole approximation code ADDA 1.3 b4*. 2014.
- [10] Patrick Christian Chaumet. “The discrete dipole approximation: A review”. In: *Mathematics* 10.17 (2022), p. 3049.
- [11] Maxim A Yurkin and Alfons G Hoekstra. “The discrete dipole approximation: an overview and recent developments”. In: *Journal of Quantitative Spectroscopy and Radiative Transfer* 106.1-3 (2007), pp. 558–589.
- [12] Patrick C Chaumet and Manuel Nieto-Vesperinas. “Time-averaged total force on a dipolar sphere in an electromagnetic field”. In: *Optics letters* 25.15 (2000), pp. 1065–1067.
- [13] OM Maragò, PH Jones, and G Volpe. *Optical tweezers: principles and applications*. 2015.
- [14] Maxim A Yurkin, Valeri P Maltsev, and Alfons G Hoekstra. “Convergence of the discrete dipole approximation. I. Theoretical analysis”. In: *JOSA A* 23.10 (2006), pp. 2578–2591.

- [15] IT Todorov, W Smith, and UK Cheshire. “The DL POLY 4 user manual”. In: *STFC, STFC Daresbury Laboratory, Daresbury, Warrington, Cheshire, WA4 4AD, United Kingdom, version 4.0* (2011).
- [16] Jens Hellmers and Thomas Wriedt. “New approaches for a light scattering Internet information portal and categorization schemes for light scattering software”. In: *Journal of Quantitative Spectroscopy and Radiative Transfer* 110.14 (2009). XI Conference on Electromagnetic and Light Scattering by Non-Spherical Particles: 2008, pp. 1511–1517. ISSN: 0022-4073. DOI: <https://doi.org/10.1016/j.jqsrt.2009.01.023>. URL: <https://www.sciencedirect.com/science/article/pii/S0022407309000284>.
- [17] Rongxin Huang et al. “Direct observation of the full transition from ballistic to diffusive Brownian motion in a liquid”. In: *Nature Physics* 7.7 (2011), pp. 576–580.
- [18] Donald L Ermak and J Andrew McCammon. “Brownian dynamics with hydrodynamic interactions”. In: *The Journal of chemical physics* 69.4 (1978), pp. 1352–1360.
- [19] Enrique J Galvez. “Gaussian beams in the optics course”. In: *American journal of physics* 74.4 (2006), pp. 355–361.
- [20] Stephen M Barnett and L Allen. “Orbital angular momentum and nonparaxial light beams”. In: *Optics communications* 110.5-6 (1994), pp. 670–678.
- [21] Alexander Jesacher et al. “Holographic optical tweezers for object manipulations at an air-liquid surface”. In: *Optics express* 14.13 (2006), pp. 6342–6352.
- [22] R. Paschotta. *Gaussian Beams*. RP Photonics Encyclopedia. Available online at https://www.rp-photonics.com/gaussian_beams.html. DOI: [10.61835/mla#title='Thislinkwillreloadthecurrentpage..](https://doi.org/10.61835/mla#title='Thislinkwillreloadthecurrentpage..) URL: https://www.rp-photonics.com/gaussian_beams.html (visited on 03/13/2025).
- [23] LibreTextsPhysics. *Energy Carried by Electromagnetic Waves*. [Online; accessed 2025-03-13]. July 2022.
- [24] Peter Bowyer. “The momentum of light in media: the Abraham-Minkowski controversy”. In: *School of Physics & Astronomy. Southampton, UK* (2005).
- [25] A Ashkin and JM Dziedzic. “Radiation pressure on a free liquid surface”. In: *Physical Review Letters* 30.4 (1973), p. 139.
- [26] GB Walker, DG Lahoz, and G Walker. “Measurement of the Abraham force in a barium titanate specimen”. In: *Canadian Journal of Physics* 53.23 (1975), pp. 2577–2586.
- [27] Robert NC Pfeifer, Timo A Nieminen, Norman R Heckenberg, and Halina Rubinsztein-Dunlop. “Colloquium: Momentum of an electromagnetic wave in dielectric media”. In: *Reviews of Modern Physics* 79.4 (2007), pp. 1197–1216.

- [28] Masud Mansuripur. “Resolution of the Abraham–Minkowski controversy”. In: *Optics Communications* 283.10 (2010), pp. 1997–2005.
- [29] H He, MEJ Friese, NR Heckenberg, and H Rubinsztein-Dunlop. “Direct observation of transfer of angular momentum to absorptive particles from a laser beam with a phase singularity”. In: *Physical review letters* 75.5 (1995), p. 826.
- [30] Stephen H Simpson et al. “Optical binding of nanowires”. In: *Nano letters* 17.6 (2017), pp. 3485–3492.
- [31] Mahito Kikumoto, Masashi Kurachi, Valer Tosa, and Hideo Tashiro. “Flexural Rigidity of Individual Microtubules Measured by a Buckling Force with Optical Traps”. In: *Biophysical Journal* 90.5 (2006), pp. 1687–1696. ISSN: 0006-3495. DOI: <https://doi.org/10.1529/biophysj.104.055483>. URL: <https://www.sciencedirect.com/science/article/pii/S0006349506723578>.
- [32] Jochen Guck et al. “The optical stretcher: a novel laser tool to micromanipulate cells”. In: *Biophysical journal* 81.2 (2001), pp. 767–784.
- [33] “Poisson’s Ratio”. In: *The Engineering ToolBox* (2008)). URL: https://www.engineeringtoolbox.com/poissons-ratio-d_1224.html.
- [34] Á González. *Measurement of areas on a sphere using Fibonacci and latitude-longitude lattices*. *Math Geosci* 42: 49–64. 2010.
- [35] ScipPy V1.15.2. 2025. URL: <https://docs.scipy.org/doc/scipy/reference/generated/scipy.spatial.ConvexHull.html>.
- [36] Edward John Routh. *An elementary treatise on the dynamics of a system of rigid bodies*. Macmillan, 1877.
- [37] myurkin dsmunev myurkin. *adda-gui*. <https://github.com/adda-team/adda-gui>. 2024.
- [38] James Paget. *Light-Driven-Deformation*. <https://github.com/James-Paget/Light-Driven-Deformation>. 2025.
- [39] Saeed Sameer Ibrahim Almishal, Tarek M Hatem, and Iman S El-Mahallawi. “A molecular dynamics study of the effect of Coulomb Buckingham Potential on equilibrium structural properties of calcium titanate perovskite”. In: *Current Applied Physics* 40 (2022), pp. 126–131.
- [40] GV Lewis and CRA Catlow. “Potential models for ionic oxides”. In: *Journal of Physics C: Solid State Physics* 18.6 (1985), p. 1149.
- [41] Stephen H Simpson and Simon Hanna. “Numerical calculation of interparticle forces arising in association with holographic assembly”. In: *JOSA A* 23.6 (2006), pp. 1419–1431.

Certification of ownership of the copyright

This Project Report is presented as part of, and in accordance with, the requirements for the degree of MSci at the University of Bristol, Faculty of Science.

I hereby assert that I own exclusive copyright in the item named below. I give permission to the University of Bristol Library to add this item to its stock and to make it available for consultation in the library, and for inter-library lending for use in another library. I also give consent for this report to be made available electronically to staff and students within the University of Bristol. It may be copied in full or in part for any bona fide library or research work. No quotation and no information derived from it may be published without the author's prior consent.

Author	James Paget
Title	Applying a bead and spring framework to light-driven deformation
Date of submission	20 th March 2025

I agree that submission of this report constitutes signing of this declaration.

This project is the property of the University of Bristol and may only be used with due regard to the rights of the author. Bibliographical references may be noted, but no part may be copied for use or quotation in any published work without the prior permission of the author. In addition, due acknowledgement for any use must be made.